1 **Assessing the simulated soil hydrothermal regime of active layer**

2 **from Noah-MP LSM v1.1 in the permafrost regions of the**

3 **Qinghai-Tibet Plateau**

4

5 Xiangfei Li[1,2,3], Tonghua Wu[1,3,*], Xiaodong Wu[1], Jie Chen[1], Sizhong, Yang[1], Xiaofan

6 Zhu[1], Guohui Zhao[2], Guojie Hu[1], Ren Li[1], Yongping Qiao[1], Cheng Yang[1,23], Junming

7 Hao[1,23], Jie Ni[1,23], Wensi Ma[1,23]

8

9 [1] Cryosphere Research Station on the Qinghai-Tibet Plateau, State Key Laboratory of

10 Cryospheric Science, Northwest Institute of Eco-Environment and Resources, Chinese

11 Academy of Sciences, Lanzhou 730000, China

12 [2] National Cryosphere Desert Data Center, Northwest Institute of Eco-Environment and

13 Resources, Chinese Academy of Sciences, Lanzhou 730000, China

14 [23] University of Chinese Academy of Sciences, Beijing 100049, China

15

16 **Correspondence:** Tonghua Wu (thuawu@lzb.ac.cn)

17

Abstract. Extensive and rigorous model inter-comparison is of great importance before application due to the uncertainties in current land surface models (LSMs). Without considering the uncertainties of forcing data and model parameters, this study designed an ensemble of 55296 experiments to evaluate the Noah land surface model with multi-parameterization (Noah-MP) for snow cover events (SCEs), soil temperature (ST) and soil liquid water (SLW) simulation, and investigated the sensitivity of parameterization schemes at a typical permafrost site on the Qinghai-Tibet Plateau. The results showed that Noah-MP systematically overestimates snow cover, which could be greatly resolved when adopting the sublimation from wind and semi-implicit snow/soil temperature time scheme. As a result of the overestimated snow, Noah-MP generally underestimates ST and ST is mostly influenced by the snow process. Systematic cold bias and large uncertainties of soil temperature remains after eliminating the effects of snow, particularly at the deep layers and during the cold season. The combination of roughness length for heat and under-canopy aerodynamic resistance contributes to resolve the cold bias of soil temperature. In addition, Noah-MP generally underestimates top SLW. The RUN process dominates the SLW simulation in comparison of the very limited impacts of all other physical processes. The analysis of the model structural uncertainties and characteristics of each scheme would be constructive to a better understanding of the land surface processes in the permafrost regions of the QTP and further model improvements towards soil hydrothermal regime modeling using the LSMs.

1 Introduction

The Qinghai-Tibet Plateau (QTP) is underlain by the world's largest high-altitude permafrost covering a contemporary area of 1.06×10^6 km^2 (Zou et al., 2017). Under the background of climate warming and intensifying human activities, soil hydrothermal dynamics in the permafrost regions on the QTP has been widely suffering from soil warming (Wang et al., 2021), soil wetting (Zhao et al., 2019), and changes in soil freeze-thaw cycle (Luo et al., 2020).Such changes has not only induced the reduction of permafrost extent, disappearing of permafrost patches and thickening of active layer (Chen et al., 2020), but also resulted in alterations in hydrological cycles (Zhao et al., 2019; Woo, 2012), changes of ecosystem (Fountain et al., 2012; Yi et al., 2011) and damages to infrastructures (Hjort et al., 2018). Therefore, it is very important to monitor and simulate the soil hydrothermal regime to adapt to the changes taking place.

A number of monitoring sites have been established in the permafrost regions of the QTP (Cao et al., 2019). However, it is inadequate to construct the soil hydrothermal state by considering the spatial variability of the ground thermal regime and an uneven distribution of these observations. In contrast, numerical models are competent alternatives. In recent years, land surface models (LSMs), which describe the exchanges of heat, water, and momentum between the land and atmosphere (Maheu et al., 2018), have received significant improvements in the representation of permafrost and frozen ground processes (Koven et al., 2013; Nicolsky et al., 2007; Melton et al., 2019). LSMs are capable of simulating the transient change of subsurface hydrothermal processes (e.g. soil temperature and moisture) with soil heat conduction (-diffusion) and water movement equations (Daniel et al., 2008). Moreover, they could be integrated with the numerical weather prediction system like WRF (Weather Research and Forecasting), making them as effective tools for comprehensive interactions between climate and permafrost (Nicolsky et al., 2007).

Some LSMs have been evaluated and applied in the permafrost regions of the QTP. Guo and Wang (2013) investigated near-surface permafrost and seasonally frozen

ground states as well as their changes using the Community Land Model, version 4 (CLM4). Hu et al. (2015) applied the coupled heat and mass transfer model to identify the hydrothermal characteristics of the permafrost active layer in the Qinghai-Tibet Plateau. Using an augmented Noah LSM, Wu et al. (2018) modeled the extent of permafrost, active layer thickness, mean annual ground temperature, depth of zero annual amplitude and ground ice content on the QTP in 2010s. Despite those achievements based on different models, LSMs are in many aspects insufficient in permafrost regions. For one thing, large uncertainties still exist in the state-of-the-art LSMs when simulating the soil hydrothermal regime on the QTP (Chen et al., 2019). For instance, 19 LSMs in CMIP5 overestimate snow depth over the QTP (Wei and Dong, 2015), which could result in the variations of the soil hydrothermal regime in the aspects of magnitude and vector (cooling or warming) (Zhang, 2005). Moreover, most of the existing LSMs are not originally developed for permafrost regions. Many of their soil processes are designed for shallow soil layers (Westermann et al., 2016), but permafrost would occur in the deep soil. And the soil column is often considered homogeneous, which cannot represent the stratified soil common on the QTP (Yang et al., 2005). Given the numerous LSMs and possible deficiencies, it is necessary to assess the parameterization schemes for permafrost modeling on the QTP, which is helpful to identify the influential sub-processes, enhance our understanding of model behavior, and guide the improvement of model physics (Zhang et al., 2016).

Noah land surface model with multi-parameterization (Noah-MP) provides a unified framework in which a given physical process can be interpreted using multiple optional parameterization schemes (Niu et al., 2011). Due to the simplicity in selecting alternative schemes within one modeling framework, it has been attracting increasing attention in inter-comparison work among multiple parameterizations at point and watershed scales (Hong et al., 2014; Zheng et al., 2017; Gan et al., 2019; Zheng et al., 2019; Chang et al., 2020; You et al., 2020). For example, Gan et al. (2019) carried out an ensemble of 288 simulations from multi-parameterization schemes of six physical processes, assessed the uncertainties of parameterizations in Noah-MP, and further

98 revealed the best-performing schemes for latent heat, sensible heat and terrestrial water

99 storage simulation over ten watersheds in China. You et al. (2020) assessed the

100 performance of Noah-MP in simulating snow process at eight sites over distinct snow

101 climates and identified the shared and specific sensitive parameterizations at all sites,

102 finding that sensitive parameterizations contribute most of the uncertainties in the

103 multi-parameterization ensemble simulations. Nevertheless, there is little research on

104 the inter-comparison of soil hydrothermal processes in the permafrost regions. In this

105 study, an ensemble experiment of totally 55296 scheme combinations was conducted

106 at a typical permafrost monitoring site on the QTP. The simulated snow cover events

107 (SCEs), soil temperature (ST) and soil liquid water (SLW) of Noah-MP model was

108 assessed and the sensitivities of parameterization schemes at different depths were

109 further investigated. This study could be expected to present a reference for soil

110 hydrothermal simulation in the permafrost regions on the QTP.

111   This article is structured as follows: Section 2 introduces the study site,

112 atmospheric forcing data, design of ensemble simulation experiments, and sensitivity

113 analysis methods. Section 3 describes the ensemble simulation results of SCEs, ST and

114 SLW, explores the sensitivity and interactions of parameterization schemes. Section 4

115 discusses the schemes in each physical process. Section 5 concludes the main findings.

116 **2   Methods and materials**

117 **2.1 Site description and observation datasets**

118   Tanggula observation station (TGL) lies in the continuous permafrost regions of

119 Tanggula Mountain, central QTP (33.07°N, 91.93°E, Alt.: 5,100 m a.s.l; Fig. 1). This

120 site a typical permafrost site on the plateau with sub-frigid and semiarid climate (Li et

121 al., 2019), filmy and discontinuous snow cover (Che et al., 2019), sparse grassland (Yao

122 et al., 2011), coarse soil (Wu and Nan, 2016; He et al., 2019), and thick active layer

123 (Luo et al., 2016), which are common features in the permafrost regions of the plateau.

124 According to the observations from 2010–2011, the annual mean air temperature of

TGL site was −4.4 °C. The annual precipitation was 375 mm, and of which 80% is concentrated between May and September. Alpine steppe with low height is the main land surface, whose coverage range is about 40% ~ 50% (Yao et al., 2011). The active layer thickness is about 3.15 m (Hu et al., 2017).

The atmospheric forcing data, including wind speed/direction, air temperature/relative humidity/pressure, downward shortwave/longwave radiation, and precipitation, were used to drive the model. These variables above were measured at a height of 2 m and covered the period from August 10, 2010 to August 10, 2012 (Beijing time) with a temporal resolution of 1 hour. Daily soil temperature and liquid moisture at depths of 5cm, 25cm, 70cm, 140cm, 220cm and 300cm from August 10, 2010 to August 9, 2011 (Beijing time) were utilized to validate the simulation results.
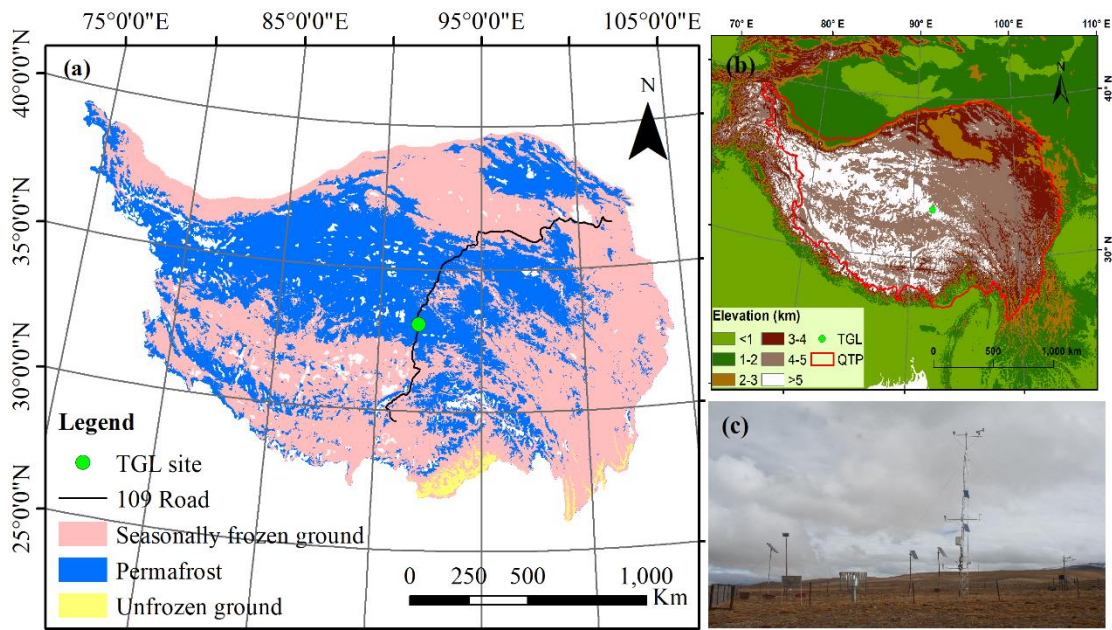
Figure 1. Location and geographic features of study site. (a) Location of observation site and permafrost distribution (Zou et al., 2017). (b) Topography of the Qinghai-Tibet Plateau. (c) Photo of the Tanggula observation station.

2.2 Ensemble experiments of Noah-MP

The offline Noah-MP LSM v1.1 was assessed in this study. The default Noah-MP consists of 12 physical processes that are interpreted by multiple optional

143   parameterization schemes. These sub-processes include vegetation model (VEG),

144   canopy stomatal resistance (CRS), soil moisture factor for stomatal resistance (BTR),

145   runoff and groundwater (RUN), surface layer drag coefficient (SFC), super-cooled

146   liquid water (FRZ), frozen soil permeability (INF), canopy gap for radiation transfer

147   (RAD), snow surface albedo (ALB), precipitation partition (SNF), lower boundary of

148   soil temperature (TBOT) and snow/soil temperature time scheme (STC) (Table 1).

149   Details about the processes and optional parameterizations can be found in Yang et al.

150   (2011a).

151   VEG(1) is adopted in the VEG process, in which the vegetation fraction is

152   prescribed according to the NESDIS/NOAA 0.144 degree monthly 5-year climatology

153   green vegetation fraction (https://www.emc.ncep.noaa.gov/mmb/gcip.html), and the

154   monthly leaf area index (LAI) was derived from the Advanced Very High-Resolution

155   Radiometer (AVHRR) (https://www.ncei.noaa.gov/data/, Claverie et al., 2016).

156   Previous studies has confirmed that Noah-MP seriously overestimate the snow events

157   and underestimate soil temperature and moisture on the QTP (Jiang et al., 2020; Li et

158   al., 2020; Wang et al., 2020), which can be greatly resolved by considering the

159   sublimation from wind (Gordon scheme) and a combination of roughness length for

160   heat and under-canopy aerodynamic resistance (Y08-UCT) (Zeng et al., 2005; Yang et

161   al., 2008; Li et al., 2020). For a more comprehensive assessment, we added two physical

162   processes based on the default Noah-MP model, i.e. the snow sublimation from wind

163   (SUB) and the combination scheme process (CMB) (Table 1). In the two processes,

164   users can choose to turn on the Gordon and Y08-UCT scheme (described in the study

165   of Li et al., 2020) or not. As a result, in total 55296 combinations are possible for the

166   13 processes and orthogonal experiments were carried out to evaluate their performance

167   in soil hydrothermal dynamics and obtain the optimal combination.

168   The Noah-MP model was modified to consider the vertical heterogeneity in the

169   soil profile by setting the corresponding soil parameters for each layer. The soil

170   hydraulic parameters, including the porosity, saturated hydraulic conductivity,

171   hydraulic potential, the Clapp-Hornberger parameter b, field capacity, wilt point, and

saturated soil water diffusivity, were determined using the pedotransfer functions proposed by Hillel (1980), Cosby et al. (1984), and Wetzel and Chang (1987) (Equations S1-S7), in which the sand and clay percentages were based on Hu et al., (2017) (Table S1). In addition, the simulation depth was extended to 8.0 m to cover the active layer thickness of the QTP. The soil column was discretized into 20 layers, whose depths follow the default scheme in CLM 5.0 (Table S1, Lawrence et al., 2018). Due to the inexact match between observed and simulated depths, the simulations at 4cm, 26cm, 80cm, 136cm, 208cm and 299cm were compared with the observations at 5cm, 25cm, 70cm, 140cm, 220cm and 300cm, respectively. A 30-year spin-up was conducted in every simulation to reach equilibrium soil states.

Table 1. The physical processes and options of Noah-MP.

Physical processes	Options
Vegetation model (VEG)	(1) table LAI, prescribed vegetation fraction
	(2) dynamic vegetation
	(3) table LAI, calculated vegetation fraction
	(4) table LAI, prescribed max vegetation fraction
Canopy stomatal resistance (CRS)	(1) Jarvis
	(2) Ball-Berry
Soil moisture factor for stomatal resistance (BTR)	(1) Noah
	(2) CLM
	(3) SSiB
Runoff and groundwater (RUN)	(1) SIMGM with groundwater
	(2) SIMTOP with equilibrium water table
	(3) Noah (free drainage)
	(4) BATS (free drainage)
Surface layer drag coefficient (SFC)	(1) Monin-Obukhov (M-O)
	(2) Chen97
Super-cooled liquid water (FRZ)	(1) generalized freezing-point depression
	(2) Variant freezing-point depression
Frozen soil permeability (INF)	(1) Defined by soil moisture, more permeable
	(2) Defined by liquid water, less permeable
Canopy gap for radiation transfer (RAD)	(1) Gap=F(3D structure, solar zenith angle)
	(2) Gap=zero
	(3) Gap=1-vegetated fraction
Snow surface albedo (ALB)	(1) BATS
	(2) CLASS
Precipitation partition (SNF)	(1) Jordan91
	(2) BATS: $T_{sfc} < T_{frz}+2.2K$
	(3) $T_{sfc} < T_{frz}$

Lower boundary of soil temperature (TBOT)	(1) zero heat flux (2) soil temperature at 8m depth
Snow/soil temperature time scheme (STC)	(1) semi-implicit (2) full implicit
Snow sublimation from wind (SUB)	(1) No (2) Yes
Combination scheme by Li et al.(2020) (CMB)	(1) No (2) Yes

183   BATS (Biosphere–Atmosphere Transfer Model); CLASS (Canadian Land Surface Scheme);

184   SIMGM (Simple topography-based runoff and Groundwater Model); SIMTOP (Simple

185   Topography-based hydrological model); SSiB (Simplified Simple Biosphere model).

186   **2.3 Methods for sensitivity analysis**

187   The simulated snow cover events (SCEs) was quantitatively evaluated using the

188   overall accuracy index (OA) (Toure et al., 2016):

189    $$\text{OA} = \frac{a + d}{a + b + c + d}$$

190   where a is the positive hits, b represents the false alarm, c is the misses, and d

191   represents the negtive hits. The value of OA range from 0 to 1. A higher OA signifies

192   better performance. Ground albedo was used as an indicator for snow events due to a

193   lack of snow depth observations. The days when the daily mean albedo is greater than

194   the observed mean value of the warm and cold season (0.25 and 0.30, respectively) are

195   identified as snow cover.

196   The root mean square error (RMSE) between the simulations and observations

197   were adopted to evaluate the performance of Noah-MP in simulating soil hydrothermal

198   dynamics.

199   To investigate the influence degrees of each physical process on SCEs, ST and

200   SLW, we firstly calculated the mean OA (for SCE) and mean RMSE (for ST and SLW)

201   ($\bar{Y}_j^i$) of the jth parameterization schemes (j = 1, 2, …) in the ith process (i = 1, 2, …).

202   Then, the maximum difference of $\bar{Y}_j^i$ ($\Delta\overline{OA}$ or $\Delta\overline{RMSE}$) was defined to quantify the

203   sensitivity of the ith process (i = 1, 2, …) (Li et al., 2015):

204    $$\Delta\overline{OA} \ or \ \Delta\overline{RMSE} = \bar{Y}_{max}^i - \bar{Y}_{min}^i$$

205 where $\bar{Y}_{max}^i$ and $\bar{Y}_{min}^i$ are the largest and the smallest $\bar{Y}_j^i$ in the ith process,

206 respectively. For a given physical process, a high $\Delta\overline{OA}$ or $\Delta\overline{RMSE}$ signifies large

207 difference between parameterizations, indicating high sensitiveness of the ith process

208 for SCEs and ST/SLW simulation.

209 The sensitivities of physical processes were determined by quantifying the

210 statistical distinction level of performance between parameterization schemes. The

211 Independent-sample T-test (2-tailed) was adopted to identify whether the distinction

212 level between two schemes is significant, and that between three or more schemes was

213 tested using the Tukey's test. Tukey's test has been widely used for its simple

214 computation and statistical features (Benjamini, 2010). The detailed descriptions about

215 this method can be found in Zhang et al. (2016), Gan et al. (2019), and You et al. (2020).

216 A process can be considered sensitive when the schemes show significant difference.

217 Moreover, schemes with large mean OA and small mean RMSE were considered

218 favorable for SCEs and ST/SLW simulation, respectively. We distinguished the

219 differences of the parameterization schemes at 95% confidence level.

220 **3   Results**

221 **3.1 General performance of the ensemble simulation**

222 The performance of Noah-MP for snow simulation was firstly tested by conducting

223 an ensemble of 55296 experiments. Due to a lack of snow depth measurements, ground

224 albedo was used as an indicator for snow cover. Figure 2 shows the monthly variations

225 of observed ground albedo and the simulations produced by the ensemble simulations.

226 The ground albedo was extremely overestimated with large uncertainties when

227 considering the snow options in Noah-MP, indicating the overestimation of snow depth

228 and duration. Such overestimation continued till July.
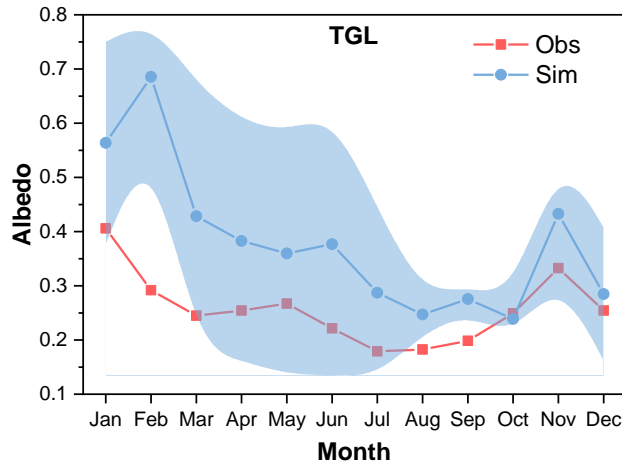
Figure 2. Monthly variations of ground albedo at TGL site for observation (Obs), and the ensemble simulation (Sim). The light blue shadow represents the standard deviation of the ensemble simulation.

Figure 3 illustrates the ensemble simulated and observed annual cycle of ST and SLW at TGL site. The ensemble experiments basically captured the seasonal variability of ST, whose magnitude decreased with soil depth. In addition, the simulated ST in the snow-affected season (October-July) showed relatively wide uncertainty ranges, particularly at the shallow layers. This indicates that the selected schemes perform much differently for snow simulation, resulting in large uncertainties of shallow STs. The simulated ST were generally smaller than the observations with relatively large gaps during the snow-affected season. It indicates that the Noah-MP model generally underestimates the ST, especially during the snow-affected months.

Since the observation equipment can only record the liquid water, soil liquid water (SLW) was evaluated against simulations from the ensemble experiments (Fig. 3). The Noah-MP model generally underestimated surface (5cm and 25cm) and deep (220cm and 300cm) SLW (Fig. 3g, 3h, 3k, 3l). However, Noah-MP tended to overestimate the SLW at the middle layers of 70cm and 140cm. Moreover, the simulated SLW exhibited relatively wide uncertainty ranges, particularly during the warm season (Fig. 3).
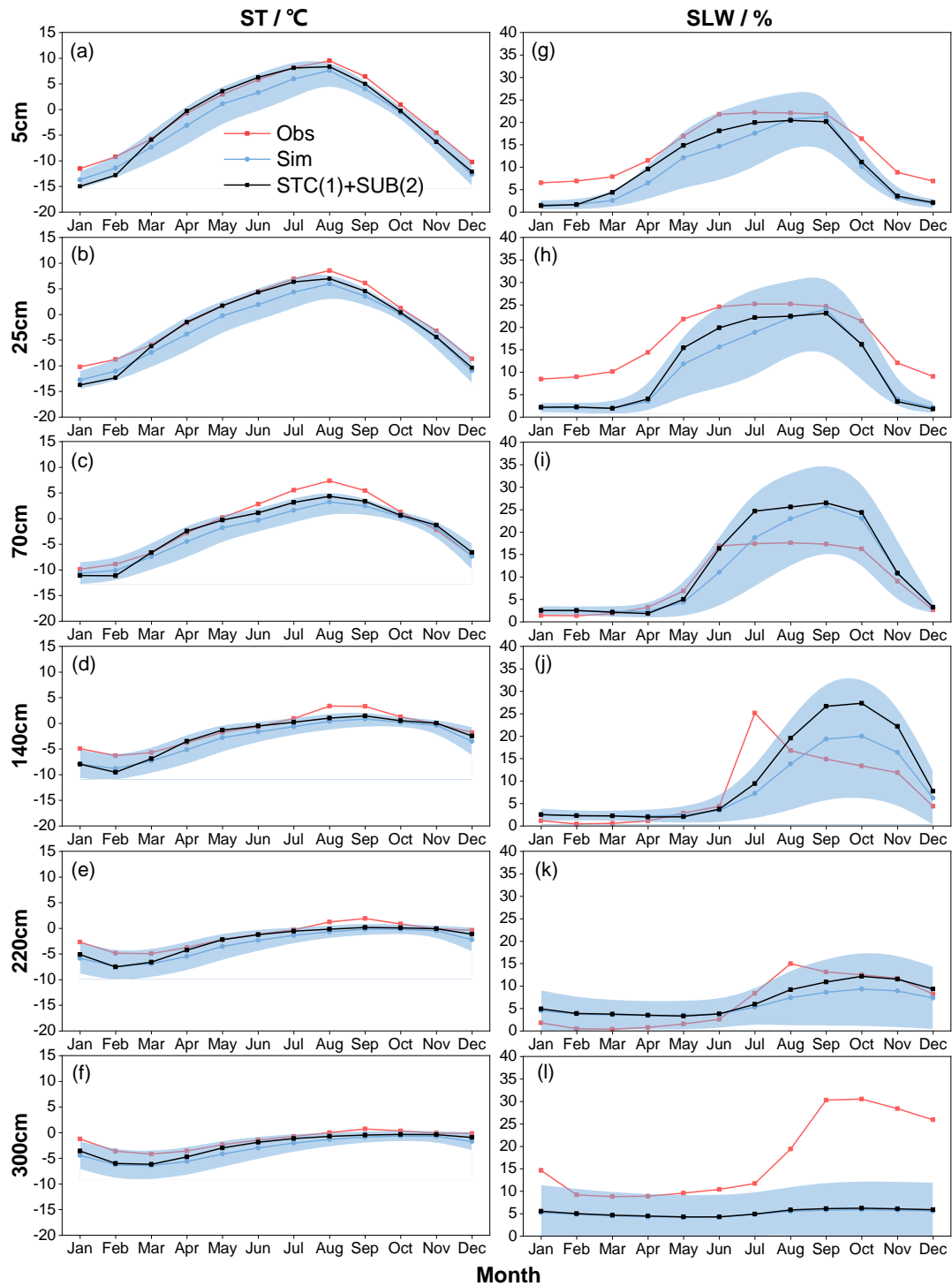
Figure 3. Monthly soil temperature (ST in °C) and soil liquid water (SLW in %) at (a, g) 5 cm, (b, h) 25 cm, (c, i) 70 cm, (d, j) 140 cm, (e, k) 220 cm, (f, l) 300 cm at TGL site. The light blue shadow represents the standard deviation of the ensemble simulation. The black line-symbol represents the ensemble mean of simulations with STC(1) and SUB(2).

3.2 Sensitivity of physical processes

3.2.1 Influence degrees of physical processes
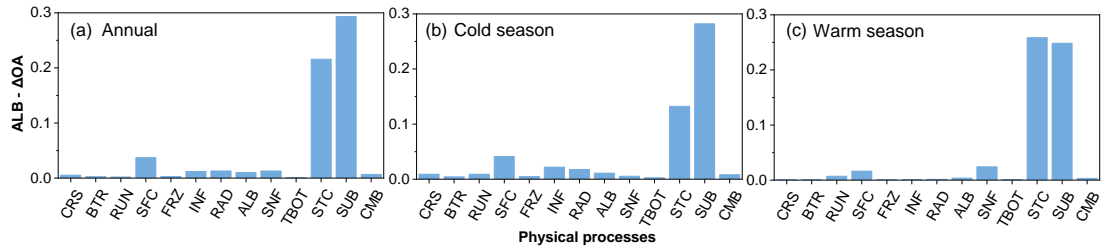
Figure 4. The maximum difference of the mean overall accuracy (OA) for albedo (ALB-ΔOA) in each physical process during the (a) annual, (b) cold season, and (c) warm season at TGL site.

Figure. 4 compares the influence scores of the 13 physical processes based on the maximum difference of the mean OA over 55296 experiments using the same scheme, for SCEs at TGL site. On the whole, the SUB and STC processes had the largest scores for the whole year as well as during both the warm and cold seasons, and the other processes showed a value less than 0.05 (Fig. 4a, 4b, 4c). Moreover, the SUB process had a consistent influence on SCEs while the influence of STC differed with season. In the cold season, the score of SUB process (0.28) was two times more than that of the STC process (Fig. 4b), indicating the relative importance of snow sublimation for SCEs simulation during the cold season. When it comes to the warm season, the influence score of SUB (0.25) did not change much, while that of STC increased to 0.26 and showed a similar influence on SCEs simulation with SUB.

272
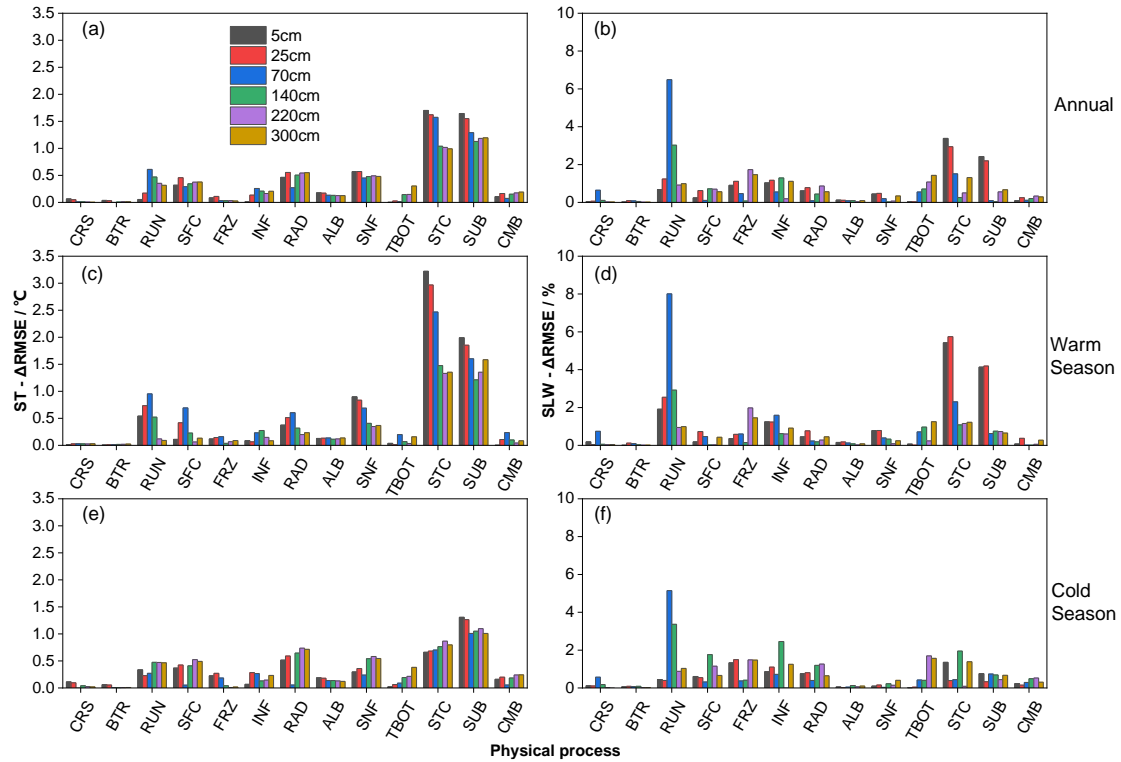
Figure 5. The maximum difference of the mean RMSE for (a, c and e) soil temperature (ST-$\Delta\overline{RMSE}$ in °C) and (b, d and f) soil liquid water (SLW-$\Delta\overline{RMSE}$ in %) in each physical process during the (a and b) annual, (c and d) warm, and (e and f) cold season at different soil depths at TGL site.

Figure. 5 compares the influence scores of the 13 physical processes at different soil depths, based on the maximum difference of the mean RMSE over 55296 experiments using the same scheme, for ST and SLW at TGL site. The snow-related processes, including the STC, SUB and SNF process showed the largest ST-$\Delta\overline{RMSE}$ at all layers, followed by the RAD, SFC and RUN processes. While the ST-$\Delta\overline{RMSE}$ of the other 7 physical processes were less than 0.5°C, among which the influence of CRS and BTR processes were negligible. What's more, the FRZ, INF, and TBOT processes had larger influence scores during the cold season than warm season, and the scores of TBOT were greater in deep soils than shallow soils. During the warm season, the physical processes generally showed more influence on shallow soil temperatures. When it comes to the cold season, the influence of the physical processes on deep layers obviously increased and comparable with that on shallow layers, implying the relatively higher uncertainties of Noah-MP during the cold season.

14

290   Most of the $\Delta\overline{RMSE}$ for SLW are less than 5%, indicating that all the physical

291   processes have limited influence on the SLW, among which CRS, BTR, ALB, SNF, and

292   CMB showed the smallest effects on SLW (Fig. 5b, 5d, 5f). During the warm season,

293   the RUN process, together with the STC and SUB processes, dominated the

294   performance of SLW simulation, especially at shallow layers (5cm, 25cm and 70cm,

295   Fig. 5d). During the cold season, however, the RUN process dominated the SLW

296   simulation with a great decline of dominance of STC and SUB processes.

297   **3.2.2 Sensitivities of physical processes and general behaviors of**

298   **parameterizations**

299   To further investigate the sensitivity of each process and the general performance

300   of the parameterizations, the Independent-sample T-test (2-tailed) and Tukey's test were

301   conducted to test whether the difference between parameterizations within a physical

302   process is significant (Fig. 6 and 7). In a given sub-process, any two schemes labelled

303   with different letters behave significantly different, and this sub-process therefore can

304   be identified as sensitive. Otherwise, the sub-process is considered insensitive. For

305   simplicity, schemes of insensitive sub-process are not labeled. Moreover, schemes with

306   the letters late in the alphabet have smaller mean RMSEs and outperform the ones with

307   the letters forward in the alphabet. Using the two schemes in CRS process (hereafter

308   CRS(1) and CRS(2)) in Fig. 6 as an example. For the annual and warm season, CRS(1)

309   and CRS(2) were labeled with "B" and "A", respectively. In the cold season, none of

310   them were labeled with letters. As described above, the CRS process was sensitive for

311   SCEs simulation during the annual and warm season, and CRS(1) outperformed

312   CRS(2). However, it was not sensitive during the cold season.

313   Consistent with the influence degrees in Fig. 4, the performance difference

314   between schemes of the STC and SUB for SCEs simulation were significantly greater

315   than other processes. Most other physical processes showed significant but limited

316   difference. Schemes in BTR and TBOT processes, however, had no significant different

317   performance. Specifically, the performance order followed STC(1) > STC(2), SUB(2) >

318   SUB(1), SFC(2) > SFC(1), ALB(2) > ALB(1), CMB(2) > CMB(1) in both annual and

seasonal scales. RAD showed no obvious difference during the warm season, while

RAD(3) outperformed RAD(1) and (2) during the cold season. For SNF, SNF(3)

generally excel SNF(1) and SNF(2), especially during the warm season.
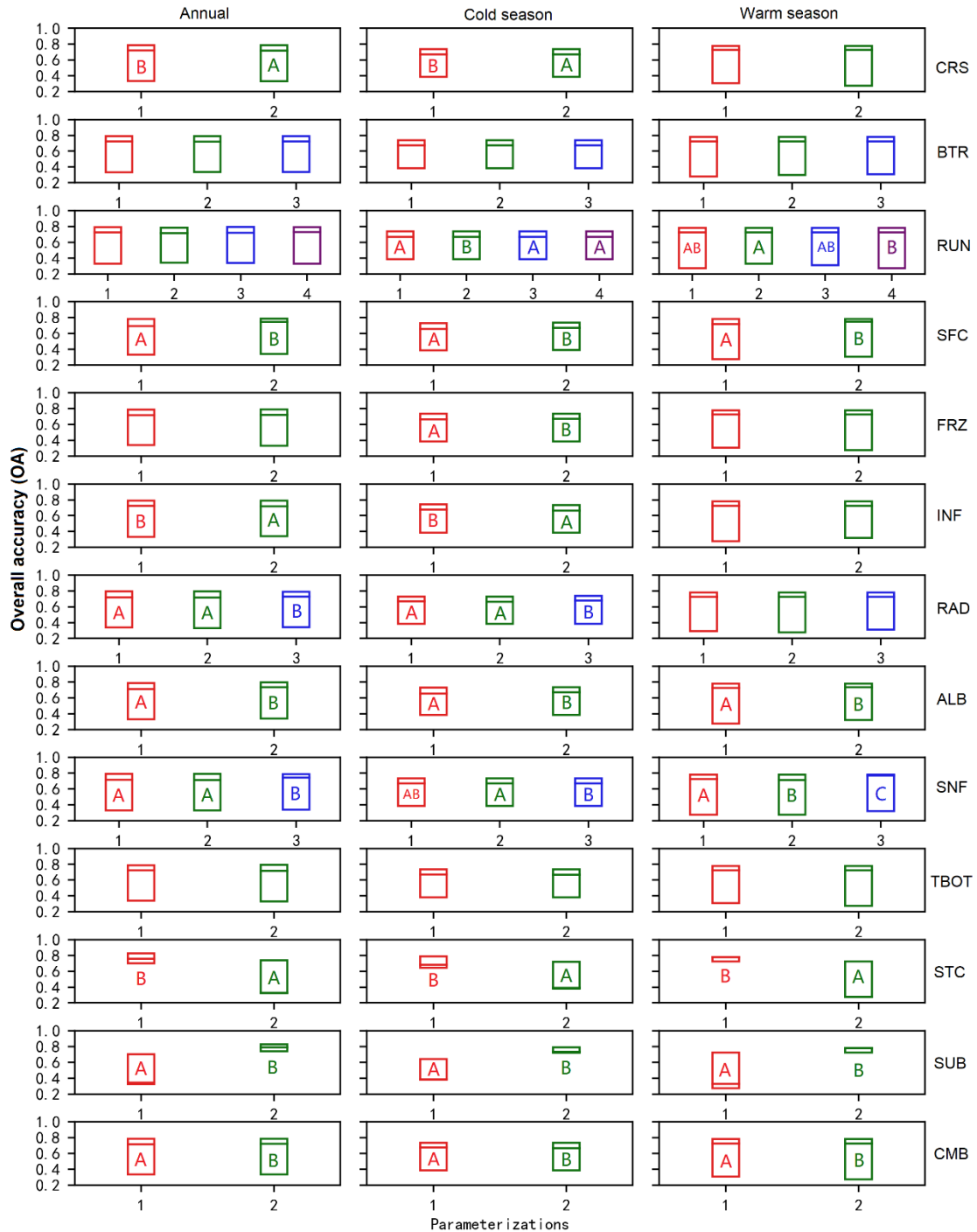
Figure 6. Distinction level for overall accuracy (OA) of snow cover events (SCEs) during the annual, warm, and cold seasons at TGL site. Limits of the boxes represent upper and lower quartiles, lines in the box indicate the median value.

All the physical processes showed sensitivities for ST and SLW simulation in

327   varying magnitudes except the BTR process and CRS process in most layers. For ST,

328   the performance difference between schemes of the STC, SUB and SNF were obviously

329   greater than other processes, indicating the importance of snow on ST, followed by the

330   RAD, SFC and RUN processes. The performance orders followed STC(1) > STC(2),

331   SUB(2) > SUB(1), SNF(3) > SNF(1) > SNF(2), RAD(3) > RAD(1) > RAD(2), and

332   SFC(2) > SFC(1). For SLW, the RUN, STC, and SUB processes showed significant and

333   higher sensitivities than other physical processes, especially during the warm season

334   and at the shallow layers (Fig. xx). Consistent with that of ST, the performance orders

335   for SLW simulation were STC(1) > STC(2), and SUB(2) > SUB(1).For the RUN

336   process, the performance orders for both ST and SLW simulation generally followed

337   RUN(4) > RUN(1) > RUN(3) > RUN(2) as a whole, among which RUN(1) and RUN(4)

338   presented similar performance during both warm and cold seasons. During both warm

339   and cold seasons, the performance orders for ST simulations were SFC(2) > SFC(1) for

340   SFC process, FRZ(2) > FRZ(1) for FRZ process, and RAD(3) > RAD(1) > RAD(2) for

341   RAD process (Fig. S2 and S3), which are particularly so for SLW simulations at shallow

342   and deep layers.

343   For ST, both FRZ and INF showed higher sensitivities during the cold season,

344   especially at shallow soils for FRZ and deep soils for INF. FRZ(2)/INF(1) outperformed

345   FRZ(1)/INF(2) for the whole year for ST simulation. Specifically, FRZ(1)/INF(2)

346   performed better at the shallow soils during the warm season while did worse during

347   the cold season compared with FRZ(2)/INF(1). For SLW, FRZ(2)/INF(2) generally

348   preceded FRZ(1)/INF(1) at shallow and deep soils (5cm, 25cm, 220cm, and 300cm)

349   while did worse at middle soil layers (140cm and 220cm).

350   For ST simulation, the performance sequence in RAD and SNF was RAD(3) >

351   RAD(1) > RAD(2) and SNF(3) > SNF (1) > SNF(2), respectively. For SLW simulation,

352   the sequence become complicated. However, RAD(3) and RAD (3) still outperformed

353   the other two schemes, respectively. ALB(2) was superior to ALB(1) for both ST and

354   SLW simulation. The influence of TBOT on soil hydrothermal arose at deep soils and

355   during cold season, and TBOT(1) excel TBOT (2). CMB(2) outperformed CMB(1) for

356 ST simulation, so did that for SLW simulation at shallow and deep soils (5cm, 25cm,

357 and 300cm).

358
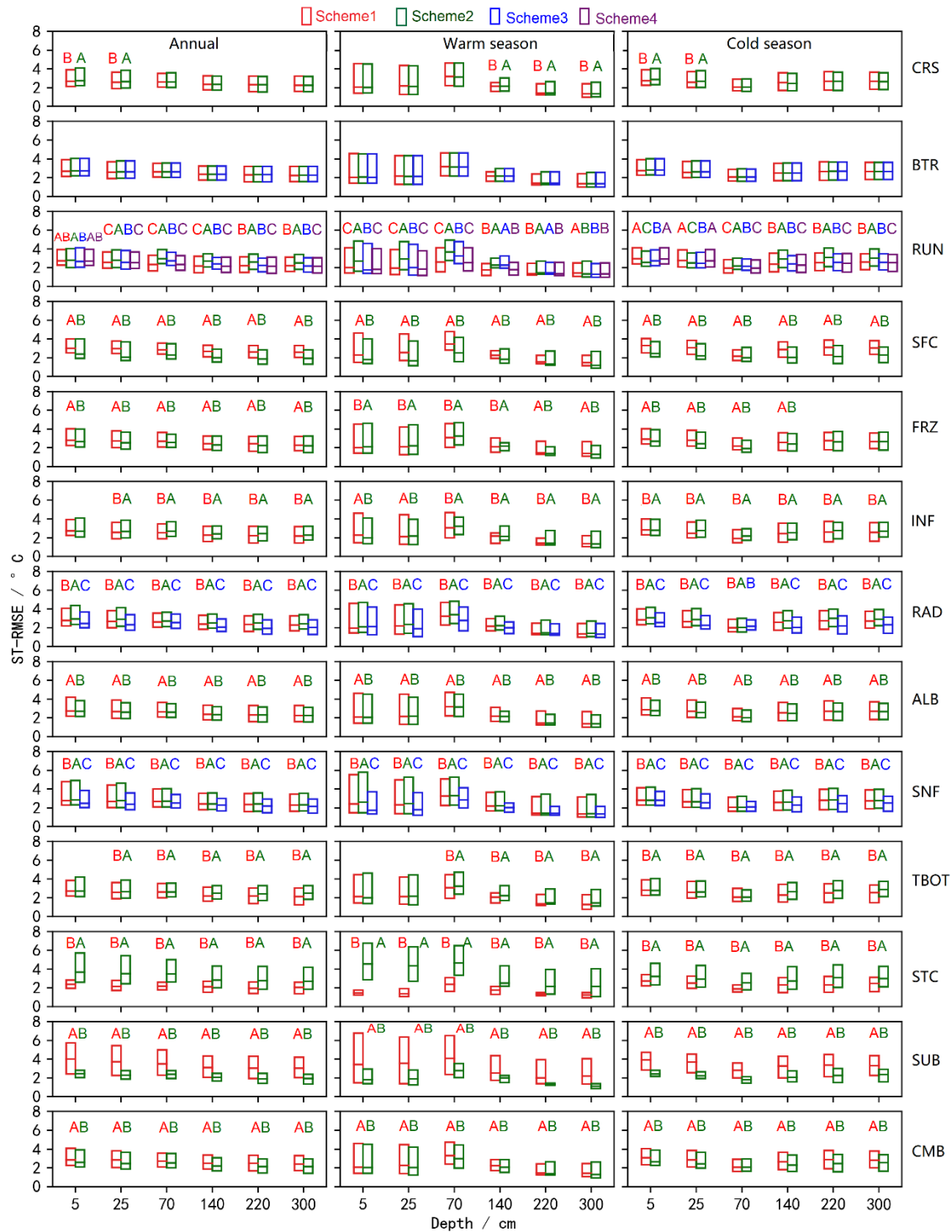
Figure 7. Distinction level for RMSE of ST at different layers during the annual, warm,

and cold seasons in the ensemble simulations at TGL site. Limits of the boxes represent

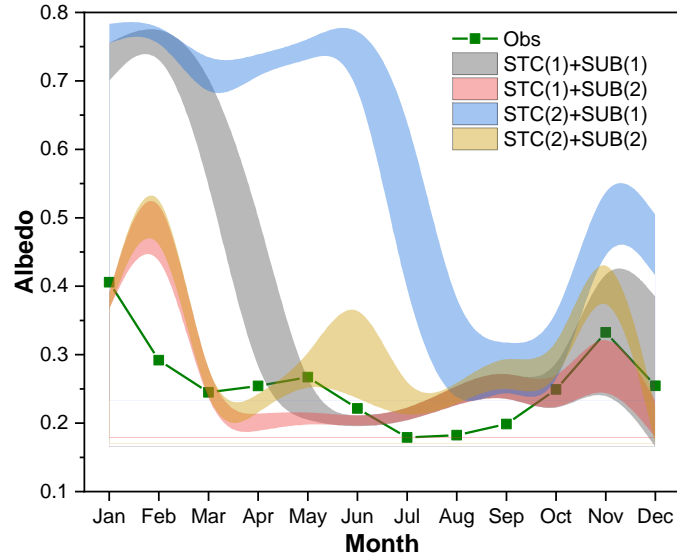upper and lower quartiles, –lines in the box indicate the median value.

18

362
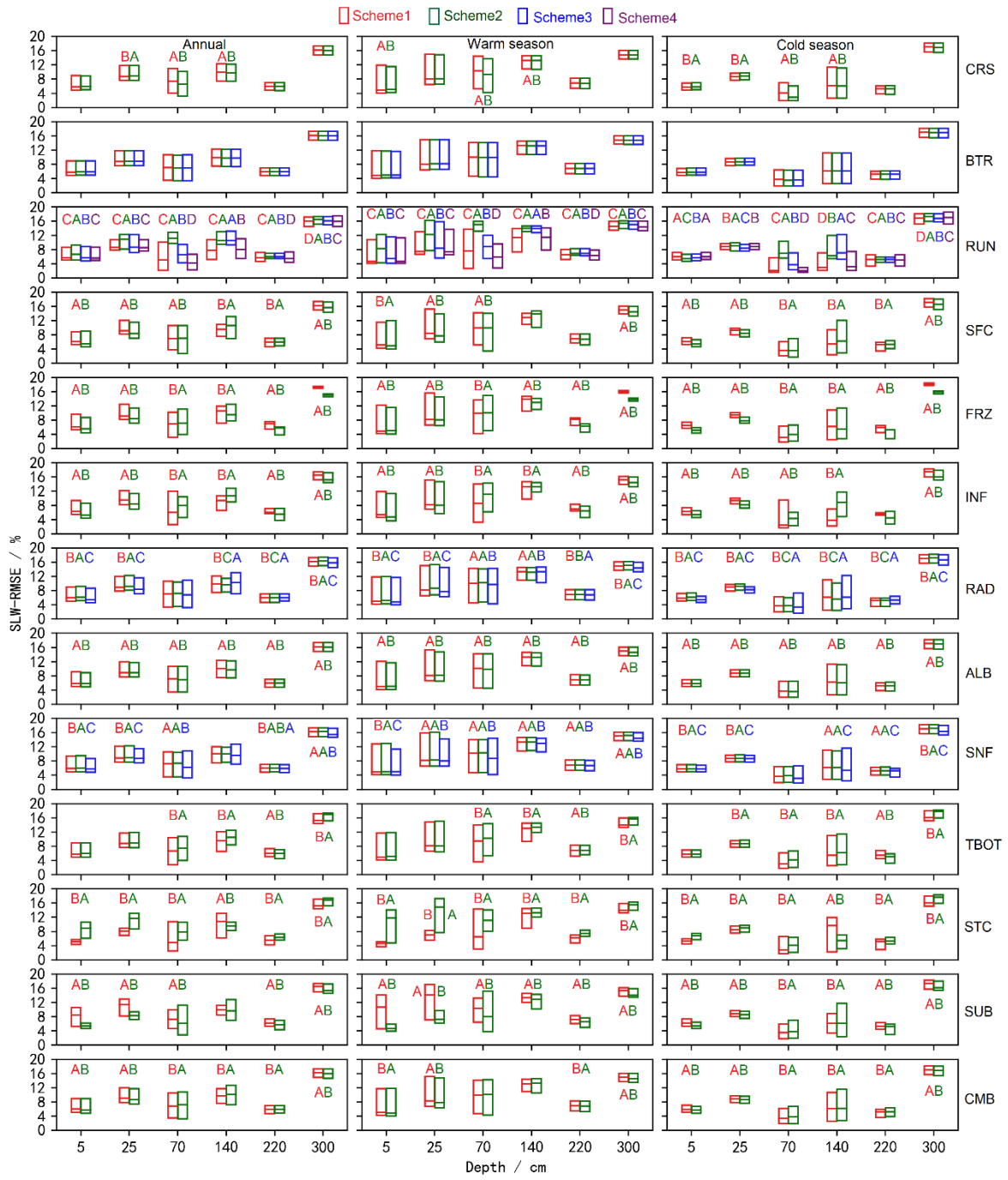
Figure 8. Same as in Figure 7 but for SLW.

3.3 Influence of snow cover and surface drag coefficient on soil hydrothermal dynamics

367

Figure 9. Uncertainty interval of ground albedo at TGL site in dominant physical processes (STC and SUB) for snow cover event simulation.

The influence of snow on soil temperature is firstly investigated. The dominant role of STC and SUB in the simulation of SCEs has been identified (Fig. 4 and 6). Interactions between the two physical processes are further analyzed here. Figure 9 compares the uncertainly intervals of the two physics. The duration of snow cover is the longest when STC(2)+SUB(1), followed when STC(2)+SUB(1). Simulations considering SUB(2) generally has a short snow duration. Among the four combinations, STC(1)+SUB(2) is in best agreement with the measurements.

Given the good performance of STC(1)+SUB(2) in simulating SCEs, the influence of snow on soil hydrothermal dynamics is investigated by comparing the total ensemble mean ST and SLW with those adopting STC(1)+SUB(2) (Fig. 3). It can be seen that the ensemble mean ST of simulations adopting STC(1) and SUB(2) are generally higher than the total ensemble means, especially during the spring and summer (Mar.-Aug.). In January and February at shallow layers (5cm, 25cm and 70cm), STC(1)+SUB(2) had a lower ST and showed an insulation effect on ST during the two months. As a whole, however, snow cover has a cooling effect on ST. In addition, along with the improved SCEs and elevated ST, STC(1)+SUB(2) induced moister soil with higher SLW (Fig. 3).
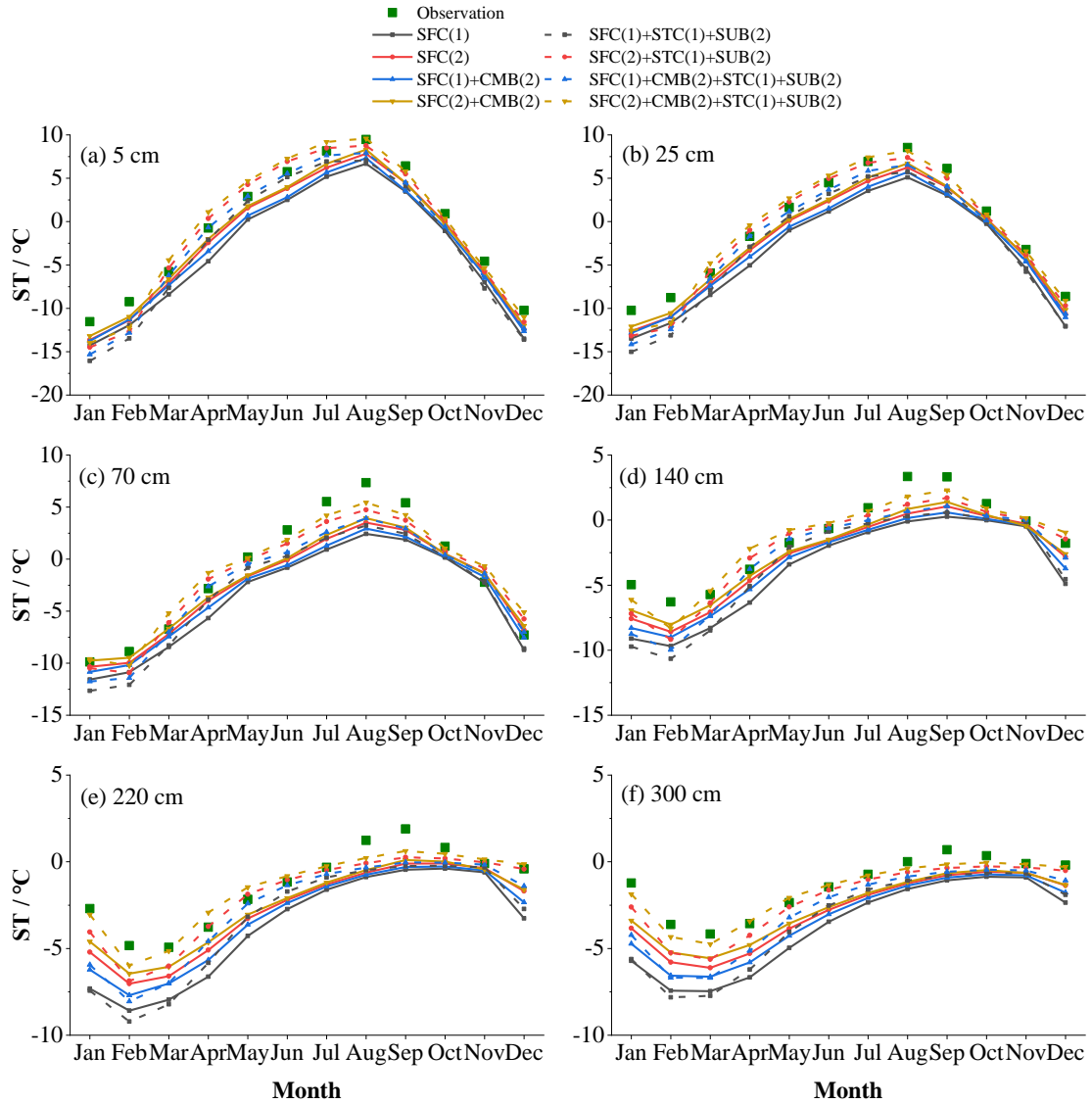
Figure 10. Monthly soil temperature (ST in °C) at (a) 5 cm, (b) 25 cm, (c) 70 cm, (d) 140 cm, (e) 220 cm, (f) 300 cm for the SFC process that consider the CMB(2) and STC(1)+SUB(2) processes or not.

SFC and CMB process using different ways to calculate the surface drag coefficient, which is of great influence for surface energy partitioning and thus ST and SLW. The influence of surface drag coefficient is assessed by comparing the soil temperature before and after considering the combined scheme (CMB(2)) and the effect of snow (STC(1)+SUB(2)) (Fig. 10). SFC(2) tended to produce higher ST than SFC(1), especially during the warming period (January-August). When adopting the combined scheme of Y08 and UCT (CMB(2)), the cold bias were significantly resolved. The performance order followed SFC(2)+CMB(2) > SFC(2) > SFC(1)+CMB(2) > SFC(1).

21

However, considerable underestimations of ST still exist at all layers due to the poor representation of snow process. After eliminating the effects of snow (STC(1)+SUB(2), dash lines in Fig. 10), the simulated ST accordingly increased except in January and February. SFC(2) and SFC(2)+CMB(2) overestimated STs from March to July at shallow layers (5cm and 25cm), resulting in good agreements of deep STs with observations. In contrast, the simulated STs at shallow layers (5cm and 25cm) by SFC(1) and SFC(1)+CMB(2) were basically consistent with observations from March to July. While large cold bias remained at deep layers.

4   Discussion

4.1 Snow cover on the QTP and its influence on soil hydrothermal regime

Snow cover in the permafrost regions of the QTP is thin, patchy, and short-lived (Che et al., 2019), whose influence on soil temperature and permafrost state is usually considered weak (Jin et al., 2008; Zou et al., 2017; Wu et al., 2018; Zhang et al., 2018; Yao et al., 2019). However, our ensemble simulations showed that the surface albedo is extremely overestimated in both magnitude and duration (Fig. 2), implying an extreme overestimation of snow cover, which is consistent with the studies using Noah-MP model (Jiang et al., 2020; Li et al., 2020; Wang et al., 2020) and widely found in other state-of-the-art LSMs (Wei and Dong, 2015) on the QTP.

Great efforts to resolve the overestimation of snow cover in LSMs include considering the vegetation effect (Park et al., 2016), the snow cover fraction (Jiang et al., 2020), the blowing snow (Xie et al., 2019), and the fresh snow albedo (Wang et al. 2020). Our results illustrated the superiority of considering the snow sublimation from wind (SUB(2)) and using semi-implicit snow/soil temperature time scheme (STC(1)) (Fig. 4, 6 and 9) when simulating snow cover on the QTP. It is consistent with previous conclusions that accounting for the loss resulting from wind contributes to improve snow cover days and depth (Yuan et al., 2016), and that STC(1) has a rapid snow ablation than STC(2) (You et al., 2020).

428   The impacts of snow cover on soil temperature in magnitude and vector (cooling or

429   warming) depend on its timing, duration, and depth (Zhang et al., 2005). In January and

430   February, the ground heat flux mainly goes upward, the warming effect of simulated

431   snow can be related to the overestimated snow depth that prevent heat loss from the

432   ground. During the spring and summer when snow melts, the cooling effects occurs,

433   mainly because considerable energy that used to heat the ground is reflected due to the

434   high albedo of snow. With the improvement of snow (STC(1)+SUB(2)), the originally

435   overestimated snow melts and infiltrated into the soil, resulting in improved SLWs (Fig.

436   3). And higher soil temperature also contributed to the SLWs according to the freezing-

437   point depression equation, in which SLW exponentially increase with soil temperature

438   for a given site (Niu and Yang, 2006).

439   **4.2 Discussions on the sensitivity of physical processes on soil hydrothermal**

440   **simulation**

441   **4.2.1 Canopy stomatal resistance (CRS) and soil moisture factor for stomatal**

442   **resistance (BTR)**

443   The biophysical process BTR and CRS directly affect the canopy stomatal

444   resistance and thus the plant transpiration (Niu et al., 2011). The transpiration of plants

445   could impact the ST/SLW through its cooling effect (Shen et al., 2015) and the water

446   balance of root zone (Chang et al., 2020). However, the annual transpiration of alpine

447   steppe is weak due to the shallow effective root zone and lower stomatal control in this

448   dry environment (Ma et al., 2015), which may explain the indistinctive or very small

449   difference among the schemes of the BTR and CRS processes for SCEs (Fig. 8), ST

450   (Fig. 7) and SLW (Fig. 8).

451   **4.2.2 Runoff and groundwater (RUN)**

452   In the warm season, different SLWs would result in the difference of the surface

453   energy partitioning and thus different soil temperatures. RUN(2) had the worst

454   performance for simulating ST and SLW (Fig. 7 and 8) among the four schemes, likely

due to its higher estimation of soil moisture (Fig. S1) and thus greater sensible heat and smaller ST (Gao et al., 2015). Likewise, RUN(4) was on a par with RUN(1) in the simulation of ST at most layers due to the very small difference in SLW of two schemes (Fig. 8 and S1). For the whole soil column, RUN(4) surpassed RUN(1) and RUN(2) for SLW simulation, both of which define surface/subsurface runoff as functions of groundwater table depth (Niu et al., 2005; Niu et al., 2007). This is in keeping with the study of Zheng et al. (2017) that soil water storage-based parameterizations outperform the groundwater table-based parameterizations in simulating the total runoff in a seasonally frozen and high-altitude Tibetan river. Besides, RUN(4) is designed based on the infiltration-excess runoff (Yang and Dickinson, 1996) in spite of the saturation-excess runoff in RUN(1) and RUN(2) (Gan et al., 2019), which is more common in arid and semiarid areas like the permafrost regions of QTP (Pilgrim et al., 1988). In the cold season, much of the liquid water freezes into ice, which would greatly influence the thermal conductivity of frozen soil considering thermal conductivity of ice is nearly four times that of the equivalent liquid water. Therefore, the impact of RUN is important for the soil temperature simulations at both warm and cold seasons (Fig. 5 and 7).

4.2.3 Surface layer drag coefficient (SFC and CMB)

SFC defines the calculations of the surface exchange coefficient for heat and water vapor (CH), which greatly impact the energy and water balance and thus the temperature and moisture of soil (Zeng et al., 2012; Zheng et al., 2012). SFC(1) adopts the Monin-Obukhov similarity theory (MOST) with a general form, while the SFC(2) uses the improved MOST modified by Chen et al. (1997). In SFC(1), the roughness length for heat (Z_{0h}) is taken as the same with the roughness length for momentum (Z_{0m}, Niu et al., 2011). SFC(2) adopts the Zilitinkevitch approach for $Z_{0,h}$ calculation (Zilitinkevich, 1995).   The difference between SFC(1) and SFC(2) has a great impact on the CH value. Several studies have reported that SFC(2) has a better performance for the simulation of sensible and latent heat on the QTP (Zhang et al., 2016; Gan et al., 2019). The results of T-test in this study showed remarkable distinctions between the two schemes, where SFC(2) was dramatically superior to SFC(1) (Fig. 7, and 8). SFC(2)

484 produces lower CH than SFC(1) (Zhang et al., 2014), resulting in less efficient

485 ventilation and greater heating of the land surface (Yang et al., 2011b), and substantial

486 improvement of the cold bias of Noah-MP in this study (Fig. 7 and 10).

487 Both SFC(1) and SFC(2) couldn't produce the diurnal variation of $Z_{0,h}$ (Chen et al.,

488 2010). CMB offers a scheme that considered the diurnal variation of $Z_{0,h}$ in bare ground

489 and under-canopy turbulent exchange in sparse vegetated surfaces (Li et al., 2020).

490 Consistent with previous studies in the QTP (Chen et al., 2010; Guo et al., 2011; Zheng

491 et al., 2015; Li et al., 2020), the simulated ST generally followed SFC(2)+CMB(2) >

492 SFC(2) > SFC(1)+CMB(2) > SFC(1) with/without removing the overestimation of

493 snow (Fig. 10), indicating that CMB(2) contributes to resolve the cold bias of LSMs.

494 However, none of the four combinations could well reproduce the shallow and deep

495 STs simultaneously. When the snow is well-simulated, SFC(2)+CMB(2) performed the

496 best at deep layers at the cost of overestimating shallow STs. Meanwhile,

497 SFC(1)+CMB(1) showed the best agreements at shallow layers with considerable cold

498 bias at deep layers, which can be related to the overestimated frozen soil thermal

499 conductivity (Luo et al., 2009; Chen et al., 2012; Li et al., 2019).

500 **4.2.4 Super-cooled liquid water (FRZ) and frozen soil permeability (INF)**

501 FRZ and INF describe the unfrozen water and permeability of frozen soil, and had

502 a larger influence on ST/SLW during the cold season than warm season as expected

503 (Fig. 5). Specifically, FRZ treats liquid water in frozen soil (super-cooled liquid water)

504 using two forms of freezing-point depression equation. FRZ(1) takes a general form

505 (Niu and Yang, 2006), while FRZ(2) exhibits a variant form that considers the increased

506 surface area of icy soil particles (Koren et al., 1999). FRZ(2) generally yields more

507 liquid water in comparison of FRZ(1) (Fig. S2). INF(1) uses soil moisture (Niu and

508 Yang, 2006) while INF(2) employs only the liquid water (Koren et al., 1999) to

509 parameterize soil hydraulic properties. INF(2) generally produces more impermeable

510 frozen soil than INF(1), which is also found in this study (Fig. S3). For the whole year,

511 INF(1) surpassed INF(2) in simulating STs, which may be related to the more realistic

512 SLWs produced by INF(1) for the whole soil column (Fig. S3).

4.2.5 Canopy gap for radiation transfer (RAD)

RAD treats the radiation transfer process within the vegetation, and adopts three methods to calculate the canopy gap. RAD(1) defines canopy gap as a function of the 3D vegetation structure and the solar zenith angle, RAD(2) employs no gap within canopy, and RAD(3) treat the canopy gap from unity minus the FVEG (Niu and Yang, 2004). The RAD(3) scheme penetrates the most solar radiation to the ground, followed by the RAD(1) and RAD(2) schemes. As an alpine grassland, there is a relative low LAI at TGL site, and thus a quite high canopy gap. So, schemes with a larger canopy gap could realistically reflect the environment. Consequently, the performance decreased in the order of RAD(3) > RAD(1) > RAD(2) for ST/SLW simulation.

4.2.6 Snow surface albedo (ALB) and precipitation partition (SNF)

The ALB describe two ways for calculating snow surface albedo, in which the ALB(1) and ALB(2) adopt the scheme from BATS and CLASS LSM, respectively. ALB(2) generally produce lower albedo than ALB(1), especially when the ground covered by snow (Fig. S4). As a result, higher net radiation absorbed by the land surface and more heat is available for heating the soil in ALB(2), which is beneficial for counteracting the cooling effect of overestimated snow on ST (Fig. S5). Along with the higher ST, ALB(2) outperformed ALB(1) for SLW simulation, likely due to more snow melt water offset the dry bias in Noah-MP (Fig. S5).

The SNF defines the snowfall fraction of precipitation as a function of surface air temperature. SNF(1) is the most complicated of the three schemes, in which the precipitation is considered rain/snow when the surface air temperature is greater/less than or equal to 2.5/0.5 °C, otherwise, it is recognized as sleet. While SNF(2) and SNF(3) simply distinguish rain or snow by judging whether the air temperature is above 2.2 °C and 0 °C or not. The significant difference between three schemes for SCEs simulation during the warm season is consistent with the large difference of snowfall fraction in this period (Fig. 6 and S6). SNF(3) is the most rigorous scheme and produce the minimum amount of snow, followed by SNF(1) and SNF(2) with limited difference (Fig. S6). This exactly explains superiority of SNF(3) for ST and SLW simulation (Fig.

542 7 and 8).

4.2.7 Lower boundary of soil temperature (TBOT) and snow/soil temperature time scheme (STC)

TBOT process adopts two schemes to describe the soil temperature boundary conditions. TBOT (1) assumes zero heat flux at the bottom of the model, while TBOT(2) adopts the soil temperature at the 8 m depth (Yang et al., 2011a). In general, TBOT(1) is expected to accumulate heat in the deep soil and produce higher ST than TBOT(2). In this study, the two assumptions performed significantly different, especially at the deep soils and during the cold season. Although TBOT(2) is more representative of the realistic condition, TBOT(1) surpassed TBOT(2) in this study. It can be related to the overall underestimation of the model, which can be alleviated by TBOT(1) because of heat accumulation (Fig. S7).

Two time discretization strategies are implemented in the STC process, where STC(1) adopts the semi-implicit scheme while STC(2) uses the full implicit scheme, to solve the thermal diffusion equation in first soil or snow layers (Yang et al., 2011a). STC(1) and STC(2) are not strictly a physical processes but different upper boundary conditions of soil column (You et al., 2019). The differences between STC(1) and STC(2) were significant (Fig. 7). The impacts of the two options on ST is remarkable (Fig. 6), particularly in the shallow layers and during the warm season (Fig. 5). In addition, STC(1) outperformed STC(2) in the ensemble simulated ST(Fig. 7), because STC(1) greatly alleviated the cold bias in Noah-MP (Fig. S8) by producing the higher OA of SCEs (Fig. 6)

4.3 Perspectives

This study analyzed the characteristics and general behaviors of each parameterization scheme of Noah-MP at a typical permafrost site on the QTP, hoping to provide a reference for simulating permafrost state on the QTP. We identified the systematic overestimation of snow cover, cold bias and dry bias in Noah-MP, and

discussed the role of snow and surface drag coefficient on soil hydrothermal dynamics. Further tests at another permafrost site (BLH site, 34.82°N, 92.92°E, Alt.: 4,659 m a.s.l) basically showed consistent conclusions with that at TGL site (see Supplementary files for details), indicating that Rrelevant results and methodologies can be practical guidelines for improving the parameterizations of physical processes and testing their uncertainties towards near-surface permafrostsoil hydrothermal modeling on in the permafrost regions of the plateau. Although the site we selected may be representative for the typical environment on the plateau, continued investigation with a broad spectrum of climate and environmental conditions is required to make a general conclusion at regional scale.

5 Conclusions

An ensemble simulation using multi-parameterizations was conducted using the Noah-MP model at the TGL site, aiming to present a reference for simulating soil hydrothermal dynamics in the permafrost regions of QTP using LSMs. The model was modified to consider the vertical heterogeneity in the soil and the simulation depth was extended to cover the whole active layer. The ensemble simulation consists of 55296 experiments, combining thirteen physical processes (CRS, BTR, RUN, SFC, FRZ, INF, RAD, ALB, SNF, TBOT, STC, SUB, and CMB) each with multiple optional schemes. On this basis, the general performance of Noah-MP was assessed by comparing simulation results with in situ observations, and the sensitivity of snow cover event, soil temperature and moisture at different depths of active layer to parameterization schemes was explored. The main conclusions are as follows:

(1) Noah-MP model tends to overestimate snow cover, which is most influenced by the STC and SUB processes. Such overestimation can be greatly resolved by considering the snow sublimation from wind (SUB(2)) and semi-implicit snow/soil temperature time scheme (STC(1)).

(2) Soil temperature is largely underestimated by the overestimated snow cover and thus dominated by the STC and SUB processes. Systematic cold bias and large

uncertainties of soil temperature still exist after eliminating the effects of snow, particularly at the deep layers and during the cold season. The combination of Y08 and UCT contributes to resolve the cold bias of soil temperature.

(3) Noah-MP tend to underestimate soil liquid water content. Most physical processes have limited influence on soil liquid water content, among which the RUN process plays a dominant role during the whole year. The STC and SUB process have a considerable influence on topsoil liquid water during the warm season.

Code availability. The source code of offline 1D Noah-MP LSM v1.1 is available at https://ral.ucar.edu/solutions/products/noah-multiparameterization-land-surface-model-noah-mp-lsm (last access: 15 May 2020). The modified Noah-MP with the consideration of vertical heterogeneity, extended soil depth, and pedotransfer functions is available upon request to the corresponding author. The data processing code are available at http://dx.doi.org/10.17632/gc7vfgkyng.1.

Data availability. The 1-hourly forcing data and daily soil temperature data at the TGL site are available at http://dx.doi.org/10.17632/gc7vfgkyng.1. Soil texture data can be obtained at https://doi.org/10.1016/j.catena.2017.04.011 (Hu et al., 2017). The AVHRR LAI data can be downloaded from https://www.ncei.noaa.gov/data/ (Claverie et al., 2016).

Author contributions. TW and XL conceived the idea and designed the model experiments. XL performed the simulations, analyzed the output, and wrote the paper. JC and GZ helped to compile the model in a Linux environment. XW, SY, XZ, GH, RL contributed to the conduction of the simulation and interpretation of the results. YQ provided the observations of atmospheric forcing and soil temperature. CY and JH helped in downloading and processing the AVHRR LAI data. JN and WM provide guidelines for the visualization. Everyone revised and polished the paper.

References

Benjamini, Y.: Simultaneous and selective inference: Current successes and future challenges, Biometrical J., 52, 708-721, https://doi.org/10.1002/bimj.200900299, 2010.

Cao, B., Zhang, T., Wu, Q., Sheng, Y., Zhao, L., and Zou, D.: Brief communication: Evaluation and inter-comparisons of Qinghai–Tibet Plateau permafrost maps based on a new inventory of field evidence, The Cryosphere, 13, 511-519, https://doi.org/10.5194/tc-13-511-2019, 2019.

Chang, M., Liao, W., Wang, X., Zhang, Q., Chen, W., Wu, Z., and Hu, Z.: An optimal ensemble of the Noah-MP land surface model for simulating surface heat fluxes over a typical subtropical forest in South China, Agric. For. Meteor., 281, 107815, https://doi.org/https://doi.org/10.1016/j.agrformet.2019.107815, 2020.

Che, T., Hao, X., Dai, L., Li, H., Huang, X., and Xiao, L.: Snow cover variation and its impacts over the Qinghai-Tibet Plateau, Bull. Chin. Acad. Sci., 34, 1247-1253, https://doi.org/10.16418/j.issn.1000-3045.2019.11.007, 2019.

Chen, F., Janjić, Z., and Mitchell, K.: Impact of atmospheric surface-layer parameterizations in the new land-surface scheme of the NCEP Mesoscale Eta Model. Boundary-Layer Meteorol. 85, 391-421, https://doi.org/10.1023/A:1000531001463, 1997.

Chen, R., Yang, M., Wang, X., and Wan, G.: Review on simulation of land-surface processes on the Tibetan Plateau, Sci. Cold Arid Reg., 11, 93-115, https://doi.org/10.3724/SP.J.1226.2019.00093, 2019.

Chen, S., Li, X., Wu, T., Xue, K., Luo, D., Wang, X., Wu, Q., Kang, S., Zhou, H., and Wei, D.: Soil thermal regime alteration under experimental warming in permafrost regions of the central Tibetan Plateau, Geoderma, 372, 114397, https://doi.org/https://doi.org/10.1016/j.geoderma.2020.114397, 2020.

Chen, Y., Yang, K., Zhou, D., Qin, J., and Guo, X.: Improving the Noah land surface model in arid regions with an appropriate parameterization of the thermal roughness length, J. Hydrometeor.,

11, 995-1006, https://doi.org/10.1175/2010JHM1185.1, 2010.

Chen, Y., Yang, K., Tang, W., Qin, J., and Zhao, L.: Parameterizing soil organic carbon's impacts on soil porosity and thermal parameters for Eastern Tibet grasslands, Sci. Chin. Earth Sci., 55, 1001-1011, https://doi.org/10.1007/s11430-012-4433-0, 2012.

Claverie, M., Matthews, J. L., Vermote, E. F., and Justice, C. O.: A 30+ year AVHRR LAI and FAPAR climate data record: Algorithm description and validation, Remote Sens., 8, 263, https://doi.org/10.3390/rs8030263, 2016.

Cosby, B. J., Hornberger, G. M., Clapp, R. B., and Ginn, T. R.: A statistical exploration of the relationships of soil moisture characteristics to the physical properties of soils, Water Resour. Res., 20, 682-690, https://doi.org/10.1029/WR020i006p00682, 1984.

Daniel, R., Nikolay, S., Bernd, E., Stephan, G., and Sergei, M.: Recent advances in permafrost modelling, Permafr. Periglac. Process., 19, 137-156, https://doi.org/doi:10.1002/ppp.615, 2008.

Fountain, A. G., Campbell, J. L., Schuur, E. A. G., Stammerjohn, S. E., Williams, M. W., and Ducklow, H. W.: The disappearing cryosphere: Impacts and ecosystem responses to rapid cryosphere loss, BioScience, 62, 405-415, https://doi.org/10.1525/bio.2012.62.4.11, 2012.

Gan, Y. J., Liang, X. Z., Duan, Q. Y., Chen, F., Li, J. D., and Zhang, Y.: Assessment and reduction of the physical parameterization uncertainty for Noah-MP land surface model, Water Resour. Res., 55, 5518-5538, https://doi.org/10.1029/2019wr024814, 2019.

Gao, Y., Kai, L., Fei, C., Jiang, Y., and Lu, C.: Assessing and improving Noah-MP land model simulations for the central Tibetan Plateau, J. Geophys. Res.-Atmos., 120, 9258-9278, https://doi.org/10.1002/2015JD023404, 2015.

Guo, D., and Wang, H.: Simulation of permafrost and seasonally frozen ground conditions on the Tibetan Plateau, 1981-2010, J. Geophys. Res.-Atmos., 118, 5216-5230, https://doi.org/10.1002/jgrd.50457, 2013.

Guo, X., Yang, K., Zhao, L., Yang, W., Li, S., Zhu, M., Yao, T., and Chen, Y.: Critical evaluation of scalar roughness length parametrizations over a melting valley glacier, Boundary-Layer Meteorol., 139(2), 307–332, https://doi.org/10.1007/s10546-010-9586-9, 2011.

He, K., Sun, J., and Chen, Q.: Response of climate and soil texture to net primary productivity and precipitation-use efficiency in the Tibetan Plateau, Pratacultural Science, 36, 1053–1065. https://doi.org/10.11829/j.issn.1001-0629.2019-0036, 2019.

Hillel, D.: Applications of Soil Physics, Academic Press, 400 pp., 1980.

Hjort, J., Karjalainen, O., Aalto, J., Westermann, S., Romanovsky, V. E., Nelson, F. E., Etzelmüller, B., and Luoto, M.: Degrading permafrost puts Arctic infrastructure at risk by mid-century, Nat. Commun., 9, 5147, https://doi.org/10.1038/s41467-018-07557-4, 2018.

Hong, S., Yu, X., Park, S. K., Choi, Y. S., and Myoung, B.: Assessing optimal set of implemented physical parameterization schemes in a multi-physics land surface model using genetic algorithm, Geosci. Model Dev., 7, 2517-2529, https://doi.org/10.5194/gmd-7-2517-2014, 2014.

Hu, G., Zhao, L., Li, R., Wu, T., Wu, X., Pang, Q., Xiao, Y., Qiao, Y., and Shi, J.: Modeling hydrothermal transfer processes in permafrost regions of Qinghai-Tibet Plateau in China, Chin. Geograph. Sci., 25, 713-727, https://doi.org/10.1007/s11769-015-0733-6, 2015.

Hu, G., Zhao, L., Wu, X., Li, R., Wu, T., Xie, C., Pang, Q., and Zou, D.: Comparison of the thermal conductivity parameterizations for a freeze-thaw algorithm with a multi-layered soil in permafrost regions, Catena, 156, 244-251, https://doi.org/10.1016/j.catena.2017.04.011, 2017.

Jiang, Y., Chen, F., Gao, Y., He, C., Barlage, M., and Huang, W.: Assessment of uncertainty sources

in snow cover simulation in the Tibetan Plateau, J. Geophys. Res.-Atmos., 125, e2020JD032674, https://doi.org/10.1029/2020JD032674, 2020.

Jin, H., Sun, L., Wang, S., He, R., Lu, L., and Yu, S.: Dual influences of local environmental variables on ground temperatures on the interior-eastern Qinghai-Tibet Plateau (I): vegetation and snow cover. J. Glaciol. Geocryol. 30, 535–545, 2008.

Koren, V., Schaake, J., Mitchell, K., Duan, Q. Y., Chen, F., and Baker, J. M.: A parameterization of snowpack and frozen ground intended for NCEP weather and climate models, J. Geophys. Res.-Atmos., 104, 19569-19585, https://doi.org/10.1029/1999JD900232, 1999.

Koven, C., Riley, W., and Stern, A.: Analysis of permafrost thermal dynamics and response to climate change in the CMIP5 earth system models, J. Clim., 26, 1877-1900, https://doi.org/10.1175/JCLI-D-12-00228.1, 2013.

Lawrence, D., Fisher, R., Koven, C., Oleson, K., Swenson, S., Vertenstein, M.: Technical description of version 5.0 of the Community Land Model (CLM), Boulder, Colorado, 2018.

Li, K., Gao, Y., Fei, C., Xu, J., Jiang, Y., Xiao, L., Li, R., and Pan, Y.: Simulation of impact of roots on soil moisture and surface fluxes over central Qinghai − Xizang Plateau. Plateau Meteor., 34, 642-652, https://doi.org/10.7522/j.issn.1000-0534.2015.00035, 2015.

Li, R., Zhao, L., Wu, T., Wang, Q. X., Ding, Y., Yao, J., Wu, X., Hu, G., Xiao, Y., Du, Y., Zhu, X., Qin, Y., Shuhua, Y., Bai, R., Erji, D., Liu, G., Zou, D., Yongping, Q., and Shi, J.: Soil thermal conductivity and its influencing factors at the Tanggula permafrost region on the Qinghai–Tibet Plateau, Agric. For. Meteor., 264, 235-246, https://doi.org/10.1016/j.agrformet.2018.10.011, 2019.

Li, X., Wu, T., Zhu, X., Jiang, Y., Hu, G., Hao, J., Ni, J., Li, R., Qiao, Y., Yang, C., Ma, W., Wen, A., and Ying, X.: Improving the Noah-MP Model for simulating hydrothermal regime of the active layer in the permafrost regions of the Qinghai-Tibet Plateau, J. Geophys. Res.-Atmos., 125, e2020JD032588, https://doi.org/10.1029/2020JD032588, 2020.

Luo, D., Wu, Q., Jin, H., Marchenko, S., Lyu, L., and Gao, S.: Recent changes in the active layer thickness across the northern hemisphere, Environ. Earth Sci., 75, 555. https://doi.org/10.1007/s12665-015-5229-2, 2016.

Luo, S., Lyu, S., Zhang, Y., Hu, Z., Ma, Y. M., Li, S. S., and Shang, L.: Soil thermal conductivity parameterization establishment and application in numerical model of central Tibetan Plateau, Chin. J. Geophys., 52, 919-928, https://doi.org/10.3969/j.issn.0001-5733.2009.04.008, 2009.

Luo, S., Wang, J., Pomeroy, J. W., and Lyu, S.: Freeze–thaw changes of seasonally frozen ground on the Tibetan Plateau from 1960 to 2014, J. Clim., 33(21), 9427-9446, https://doi.org/10.1175/JCLI-D-19-0923.1, 2020.

Ma, N., Zhang, Y., Guo, Y., Gao, H., Zhang, H., and Wang, Y.: Environmental and biophysical controls on the evapotranspiration over the highest alpine steppe, J. Hydrol., 529, 980-992, https://doi.org/https://doi.org/10.1016/j.jhydrol.2015.09.013, 2015.

Maheu, A., Anctil, F., Gaborit, É., Fortin, V., Nadeau, D. F., and Therrien, R.: A field evaluation of soil moisture modelling with the Soil, Vegetation, and Snow (SVS) land surface model using evapotranspiration observations as forcing data, J. Hydrol., 558, 532-545, https://doi.org/https://doi.org/10.1016/j.jhydrol.2018.01.065, 2018.

Melton, J., Verseghy, D., Sospedra-Alfonso, R., and Gruber, S.: Improving permafrost physics in the coupled Canadian Land Surface Scheme (v.3.6.2) and Canadian Terrestrial Ecosystem Model (v.2.1) (CLASS-CTEM), Geosci. Model Dev., 12, 4443-4467, https://doi.org/10.5194/gmd-12-

4443-2019, 2019.

Nicolsky, D. J., Romanovsky, V. E., Alexeev, V. A., and Lawrence, D. M.: Improved modeling of permafrost dynamics in a GCM land-surface scheme, Geophys. Res. Lett., 34, L08501, https://doi.org/10.1029/2007gl029525, 2007.

Niu, G.-Y., and Yang, Z.-L.: Effects of vegetation canopy processes on snow surface energy and mass balances, J. Geophys. Res.-Atmos., 109, D23111, https://doi.org/10.1029/2004jd004884, 2004.

Niu, G.-Y., and Yang, Z.-L.: Effects of frozen soil on snowmelt runoff and soil water storage at a continental scale, J. Hydrometeor., 7, 937-952, https://doi.org/10.1175/JHM538.1, 2006.

Niu, G.-Y., Yang, Z.-L., Dickinson, R. E., and Gulden, L. E.: A simple TOPMODEL-based runoff parameterization (SIMTOP) for use in global climate models, J. Geophys. Res.-Atmos., 110, D21106, https://doi.org/10.1029/2005jd006111, 2005.

Niu, G.-Y., Yang, Z.-L., Dickinson, R. E., Gulden, L. E., and Su, H.: Development of a simple groundwater model for use in climate models and evaluation with Gravity Recovery and Climate Experiment data, J. Geophys. Res.-Atmos., 112, D07103, https://doi.org/10.1029/2006jd007522, 2007.

Niu, G.-Y., Yang, Z.-L., Mitchell, K. E., Chen, F., Ek, M. B., Barlage, M., Kumar, A., Manning, K., Niyogi, D., and Rosero, E.: The community Noah land surface model with multiparameterization options (Noah-MP): 1. Model description and evaluation with local-scale measurements, J. Geophys. Res.-Atmos., 116, D12109, https://doi.org/10.1029/2010JD015139, 2011.

Park, S., and Park, S.K.: Parameterization of the snow-covered surface albedo in the Noah-MP Version 1.0 by implementing vegetation effects, Geosci. Model Dev. 9, 1073-1085, https://doi.org/10.5194/gmd-9-1073-2016, 2016.

Pilgrim, D. H., Chapman, T. G., and Doran, D. G.: Problems of rainfall-runoff modelling in arid and semiarid regions, Hydrolog. Sci. J., 33, 379-400, https://doi.org/10.1080/02626668809491261, 1988.

Qin, Y., Wu, T., Zhao, L., Wu, X., Li, R., Xie, C., Pang, Q., Hu, G., Qiao, Y., Zhao, G., Liu, G., Zhu, X., and Hao, J.: Numerical modeling of the active layer thickness and permafrost thermal state across Qinghai-Tibetan Plateau. J. Geophys. Res.-Atmos., 122, 11,604-611,620, https://doi.org/10.1002/2017JD026858, 2017.

Schaake, J. C., Koren, V. I., Duan, Q. Y., Mitchell, K., and Chen, F.: Simple water balance model for estimating runoff at different spatial and temporal scales, J. Geophys. Res.-Atmos., 101, 7461-7475, https://doi.org/10.1029/95jd02892, 1996.

Shen, M., Piao, S., Jeong, S.-J., Zhou, L., Zeng, Z., Ciais, P., Chen, D., Huang, M., Jin, C.-S., Li, L. Z. X., Li, Y., Myneni, R. B., Yang, K., Zhang, G., Zhang, Y., and Yao, T.: Evaporative cooling over the Tibetan Plateau induced by vegetation growth, Proc. Natl. Acad. Sci. U. S. A., 112, 9299-9304, https://doi.org/10.1073/pnas.1504418112, 2015.

Toure, A., Rodell, M., Yang, Z., Beaudoing, H., Kim, E., Zhang, Y., and Kwon, Y.: Evaluation of the snow simulations from the community land model, version 4 (CLM4). J. Hydrometeor., 17, 153–170, https://doi.org/10.1175/JHM-D-14-0165.1, 2016.

Wang, X., Chen, R., Han, C., Yang, Y., Liu, J., Liu, Z., Guo, S., and Song, Y.: Response of shallow soil temperature to climate change on the Qinghai–Tibetan Plateau, Int. J. Climatol., 41, 1-16, https://doi.org/10.1002/joc.6605, 2021.

Wang, W., Yang, K., Zhao, L., Zheng, Z., Lu, H., Mamtimin, A., Ding, B., Li, X., Zhao, L., Li, H.,

Che, T., and Moore, J. C.: Characterizing surface albedo of shallow fresh snow and its importance for snow ablation on the interior of the Tibetan Plateau, J. Hydrometeor., 21, 815-827, https://doi.org/10.1175/JHM-D-19-0193.1, 2020.

Wei, Z., and Dong, W.: Assessment of simulations of snow depth in the Qinghai-Tibetan Plateau using CMIP5 multi-models, Arct. Antarct. Alp. Res., 47, 611-525, https://doi.org/10.1657/AAAR0014-050, 2015.

Westermann, S., Langer, M., Boike, J., Heikenfeld, M., Peter, M., Etzelmuller, B., and Krinner, G.: Simulating the thermal regime and thaw processes of ice-rich permafrost ground with the land-surface model CryoGrid 3, Geosci. Model Dev., 9, 523-546, https://doi.org/10.5194/gmd-9-523-2016, 2016.

Wetzel, P., and Chang, J.-T.: Concerning the relationship between evapotranspiration and soil moisture, J. Clim. Appl. Meteorol., 26, 18-27, https://doi.org/10.1175/1520-0450(1987)026<0018:CTRBEA>2.0.CO;2, 1987.

Woo, M. K.: Permafrost Hydrology, Springer, Berlin, Heidelberg, 2012.

Wu, X., and Nan, Z.: A multilayer soil texture dataset for permafrost modeling over Qinghai-Tibetan Plateau. Paper presented at 2016 IEEE International Geoscience and Remote Sensing Symposium (IGARSS), Beijing, China. https://doi.org/10.1109/IGARSS.2016.7730283, 2016.

Wu, X. B., Nan, Z. T., Zhao, S. P., Zhao, L., and Cheng, G. D.: Spatial modeling of permafrost distribution and properties on the Qinghai-Tibet Plateau, Permafr. Periglac. Process., 29, 86-99, https://doi.org/10.1002/ppp.1971, 2018.

Xie, Z., Hu, Z., Ma, Y., Sun, G., Gu, L., Liu, S., Wang, Y., Zheng, H., and Ma, W.: Modeling blowing snow over the Tibetan Plateau with the community land model: Method and preliminary evaluation, J. Geophys. Res.-Atmos., 124, 9332–9355, https://doi.org/10.1029/2019jd030684, 2019.

Yang, K., Koike, T., Ye, B., and Bastidas, L.: Inverse analysis of the role of soil vertical heterogeneity in controlling surface soil state and energy partition, J. Geophys. Res.-Atmos., 110, D08101, https://doi.org/10.1029/2004jd005500, 2005.

Yang, K., Koike, T., Ishikawa, H., Kim, J., Li, X., Liu, H., Shaomin, L., Ma, Y., and Wang, J.: Turbulent flux transfer over bare-soil surfaces: Characteristics and parameterization, J. Appl. Meteorol. Clim., 47, 276-290, https://doi.org/10.1175/2007JAMC1547.1, 2008.

Yang, Z.-L., and Dickinson, R. E.: Description of the biosphere-atmosphere transfer scheme (BATS) for the soil moisture workshop and evaluation of its performance, Global Planet. Change, 13, 117-134, https://doi.org/10.1016/0921-8181(95)00041-0, 1996.

Yang, Z.-L., Cai, X., Zhang, G., Tavakoly, A., Jin, Q., Meyer, L., and Guan, X.: The Community Noah Land Surface Model with Multi-Parameterization Options (Noah-MP): Technical Description, 2011a.

Yang, Z.-L., Niu, G.-Y., E. Mitchell, K., Chen, F., B. Ek, M., Barlage, M., Longuevergne, L., Manning, K., Niyogi, D., Tewari, M., and Xia, Y.: The community Noah land surface model with multiparameterization options (Noah-MP): 2. Evaluation over global river basins. J. Geophys. Res.-Atmos. 116, D12110, https://doi.org/10.1029/2010JD015140, 2011b.

Yao, C., Lyu, S., Wang, T., Wang, J., and Ma, C.: Analysis on freezing-thawing characteristics of soil in high and low snowfall years in source region of the Yellow River, Plateau Meteor., 38, 474-483, 2019.

Yao, J., Zhao, L., Gu, L., Qiao, Y., and Jiao, K.: The surface energy budget in the permafrost region

of the Tibetan Plateau, Atmos. Res., 102, 394-407, https://doi.org/https://doi.org/10.1016/j.atmosres.2011.09.001, 2011.

Yi, S., Zhou, Z., Ren, S., Ming, X., Yu, Q., Shengyun, C., and Baisheng, Y.: Effects of permafrost degradation on alpine grassland in a semi-arid basin on the Qinghai–Tibetan Plateau, Environ. Res. Lett., 6, 045403, https://doi.org/10.1088/1748-9326/6/4/045403, 2011.

You, Y., Huang, C., Gu, J., Li, H., Hao, X., and Hou, J.: Assessing snow simulation performance of typical combination schemes within Noah-MP in northern Xinjiang, China, J. Hydro., 581, 124380, https://doi.org/10.1016/j.jhydrol.2019.124380, 2020.

You, Y., Huang, C., Yang, Z., Zhang, Y., Bai, Y., and Gu, J.: Assessing Noah-MP parameterization sensitivity and uncertainty interval across snow climates, J. Geophys. Res.-Atmos., 125, e2019JD030417, https://doi.org/10.1029/2019jd030417, 2020.

Yuan, W., Xu, W., Ma, M., Chen, S., Liu, W., and Cui, L.: Improved snow cover model in terrestrial ecosystem models over the Qinghai–Tibetan Plateau, Agric. For. Meteor., 218-219, 161-170, https://doi.org/10.1016/j.agrformet.2015.12.004, 2016.

Zeng, X., Wang, Z., and Wang, A.: Surface skin temperature and the interplay between sensible and ground heat fluxes over arid regions, J. Hydrometeor., 13, 1359-1370, https://doi.org/10.1175/JHM-D-11-0117.1, 2012.

Zhang, G., Chen, F., and Gan, Y.: Assessing uncertainties in the Noah-MP ensemble simulations of a cropland site during the Tibet Joint International Cooperation program field campaign, J. Geophys. Res.-Atmos., 121, 9576-9596, https://doi.org/10.1002/2016jd024928, 2016.

Zhang, H., Su. Y., Jiang, H., Chao, H., and Su, W.: Influence of snow subliming process on land-atmosphere interaction at alpine wetland, J. Glaci. Geocry., 40, 1223-1230, 2018.

Zhang, T.: Influence of the seasonal snow cover on the ground thermal regime: An overview, Reviews of Geophysics, 43, RG4002, https://doi.org/10.1029/2004RG000157, 2005.

Zhao, L., Hu, G., Zou, D., Wu, X., Ma, L., Sun, Z., Yuan, L., Zhou, H., and Liu, S.: Permafrost changes and its effects on hydrological processes on Qinghai-Tibet Plateau, Bull. Chin. Acad. Sci., 34, 1233-1246, https://doi.org/10.16418/j.issn.1000-3045.2019.11.006, 2019.

Zeng, X., Dicknson, R., Barlage, M., Dai, Y., Wang, G., and Oleson, K.: Treatment of undercanopy turbulence in land models. J. Clim., 18(23), 5086–5094. https://doi.org/10.1175/Jcli3595.1, 2005.

Zheng, D., van der Velde, R., Su, Z., Wen, J., Booij, M., Hoekstra, A., and Wang, X.: Under-canopy turbulence and root water uptake of a Tibetan meadow ecosystem modeled by Noah-MP, Water Resour. Res., 51, 5735–5755. https://doi.org/10.1002/2015WR017115, 2015.

Zheng, D., van der Velde, R., Su, Z., Wen, J., and Wang, X.: Assessment of Noah land surface model with various runoff parameterizations over a Tibetan river, J. Geophys. Res.-Atmos., 122, 1488-1504, https://doi.org/10.1002/2016jd025572, 2017.

Zheng, H., Yang, Z.-L., Lin, P., Wei, J., Wu, W.-Y., Li, L., Zhao, L., and Wang, S.: On the sensitivity of the precipitation partitioning into evapotranspiration and runoff in land surface parameterizations, Water Resour. Res., 55, 95-111, https://doi.org/10.1029/2017WR022236, 2019.

Zheng, W., Wei, H., Wang, Z., Zeng, X., Meng, J., Ek, M., Mitchell, K., and Derber, J.: Improvement of daytime land surface skin temperature over arid regions in the NCEP GFS model and its impact on satellite data assimilation, J. Geophys. Res.-Atmos., 117, D06117, https://doi.org/10.1029/2011jd015901, 2012.

Zilitinkevich, S.: Non-local turbulent transport pollution dispersion aspects of coherent structure of

882   convective flows, Air Pollution III, Air pollution theory and simulation (H Power, N
883   Moussiopoulos, C A Brebbia, eds) Computational Mechanics Publ , Southampton, Boston, 1, 53-
884   60, 1995.
885   Zou, D., Zhao, L., Sheng, Y., Chen, J., Hu, G., Wu, T., Wu, J., Xie, C., Wu, X., Pang, Q., Wang, W.,
886   Du, E., Li, W., Liu, G., Li, J., Qin, Y., Qiao, Y., Wang, Z., Shi, J., and Cheng, G.: A new map of
887   permafrost distribution on the Tibetan Plateau, The Cryosphere, 11, 2527-2542,
888   https://doi.org/10.5194/tc-11-2527-2017, 2017.
889

Supplement of

Assessing the simulated soil hydrothermal regime of active layer from Noah-MP LSM v1.1 in the permafrost regions of the Qinghai-Tibet Plateau

Xiangfei Li et al.

Correspondence to: Tonghua Wu (thuawu@lzb.ac.cn)

Content: Equations S1-S7; Table S1; Figures S1-S~~8~~17

The soil hydraulic parameters of each layer, including the porosity (θ_s), saturated hydraulic conductivity (K_s), hydraulic potential (ψ_s), the Clapp-Hornberger parameter (b), field capacity (θ_{ref}), wilt point (θ_w), and saturated soil water diffusivity (D_s), were determined using the pedotransfer functions proposed by Hillel (1980), Cosby et al. (1984), and Wetzel and Chang (1987):

$$\theta_s = 0.489 - 0.00126(\%sand) \tag{S1}$$

$$K_s = 7.0556 \times 10^{-6.884+0.0153(\%sand)} \tag{S2}$$

$$\psi_s = -0.01 \times 10^{1.88-0.0131(\%sand)} \tag{S3}$$

$$b = 2.91 + 0.159(\%clay) \tag{S4}$$

$$\theta_{ref} = \theta_s \left[\frac{1}{3} + \frac{2}{3} \left(\frac{5.79 \times 10^{-9}}{K_s} \right)^{1/(2b+3)} \right] \tag{S5}$$

$$\theta_w = 0.5\theta_s \left(\frac{-200}{\psi_s} \right)^{-1/b} \tag{S6}$$

$$D_s = b \cdot K_s \cdot \left(\frac{\psi_s}{\theta_s} \right) \tag{S7}$$

where $\%sand$ and $\%clay$ represent the percentage (%) of sand and clay content in soil, respectively.

Table S1 Soil discretization scheme and soil particle fraction in this study.

Layer	Z_i	ΔZ_i	$Z_{h,i}$	Sand (%)	Silt (%)	Clay (%)
1	0.010	0.020	0.020			
2	0.040	0.040	0.060	85.48	12.59	1.93
3	0.090	0.060	0.120			
4	0.160	0.080	0.200	83.51	13.57	2.92
5	0.260	0.120	0.320	81.15	15.58	3.27
6	0.400	0.160	0.480	86.62	11.16	2.22
7	0.580	0.200	0.680	78.73	18.06	3.21
8	0.800	0.240	0.920	88.12	8.98	2.90
9	1.060	0.280	1.200	95.00	3.00	2.00
10	1.360	0.320	1.520			
11	1.700	0.360	1.880	92.50	4.00	3.50
12	2.080	0.400	2.280	90.00	5.00	5.00
13	2.500	0.440	2.720			
14	2.990	0.540	3.260			
15	3.580	0.640	3.900			
16	4.270	0.740	4.640	68.00	20.00	12.00
17	5.060	0.840	5.480			
18	5.950	0.940	6.420			
19	6.940	1.040	7.460			
20	7.980	1.040	8.500			

Layer node depth (Z_i), thickness (ΔZ_i), and depth at layer interface ($Z_{h,i}$) for default soil column. All in meters.
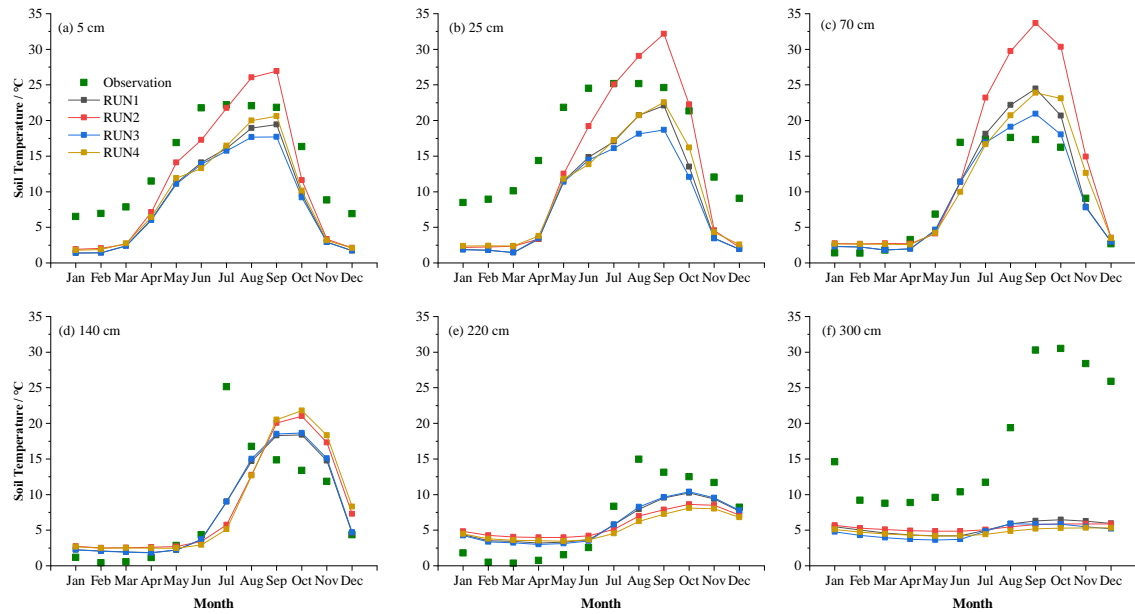
Figure. S1 Monthly soil liquid water (SLW in %) at (a) 5 cm, (b) 25 cm, (c) 70 cm, (d) 140 cm, (e) 220 cm, (f) 300 cm for the RUN process.
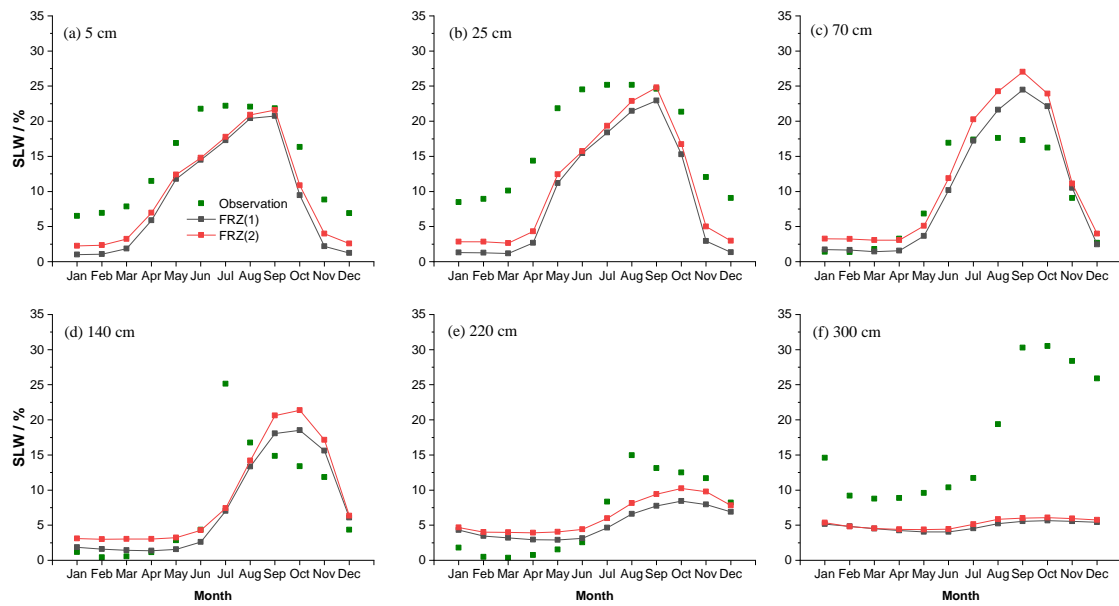

Figure. S2 Monthly soil liquid water (SLW in %) at (a) 5 cm, (b) 25 cm, (c) 70 cm, (d) 140 cm, (e) 220 cm, (f) 300 cm for the FRZ process.
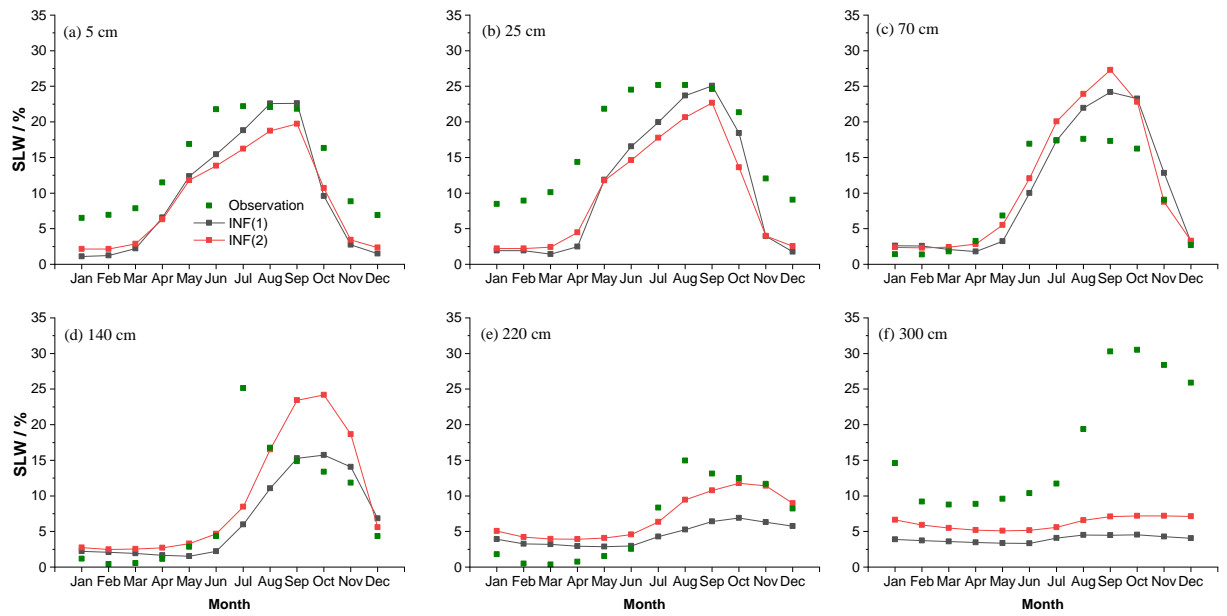
Figure. S3 Monthly soil liquid water (SLW in %) at (a) 5 cm, (b) 25 cm, (c) 70 cm, (d) 140 cm, (e) 220 cm, (f) 300 cm for the INF process.
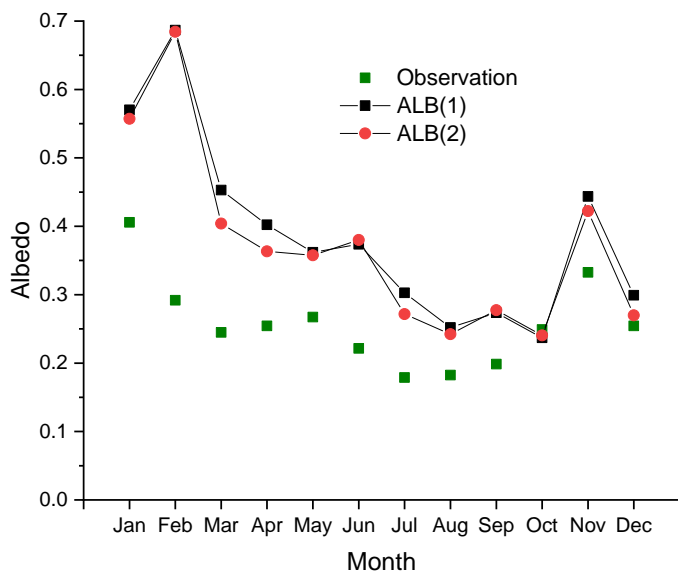
Figure. S4 Monthly ground albedo for the ALB process.
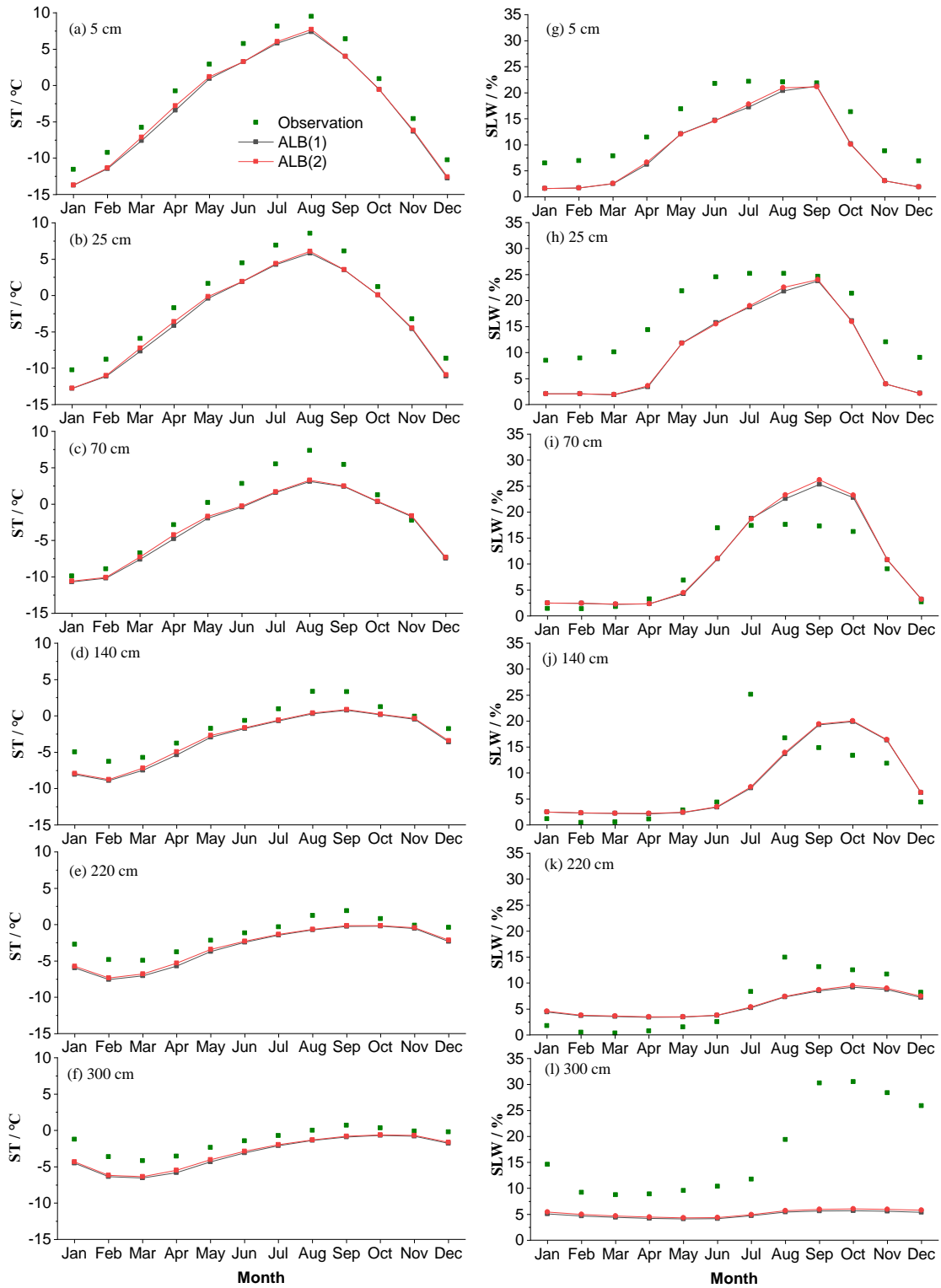
Figure. S5 Monthly soil temperature (ST in °C) and liquid water (SLW in %) at (a, g) 5 cm, (b, h) 25 cm, (c, i) 70 cm, (d, j) 140 cm, (e, k) 220 cm, (f, l) 300 cm for the ALB process.
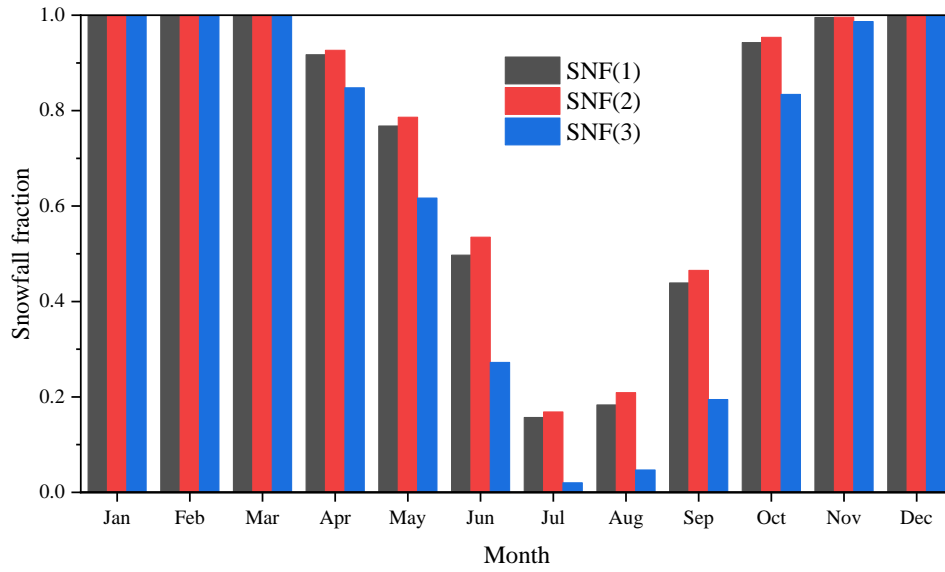
Figure. S6 Monthly snowfall fraction for the SNF process.
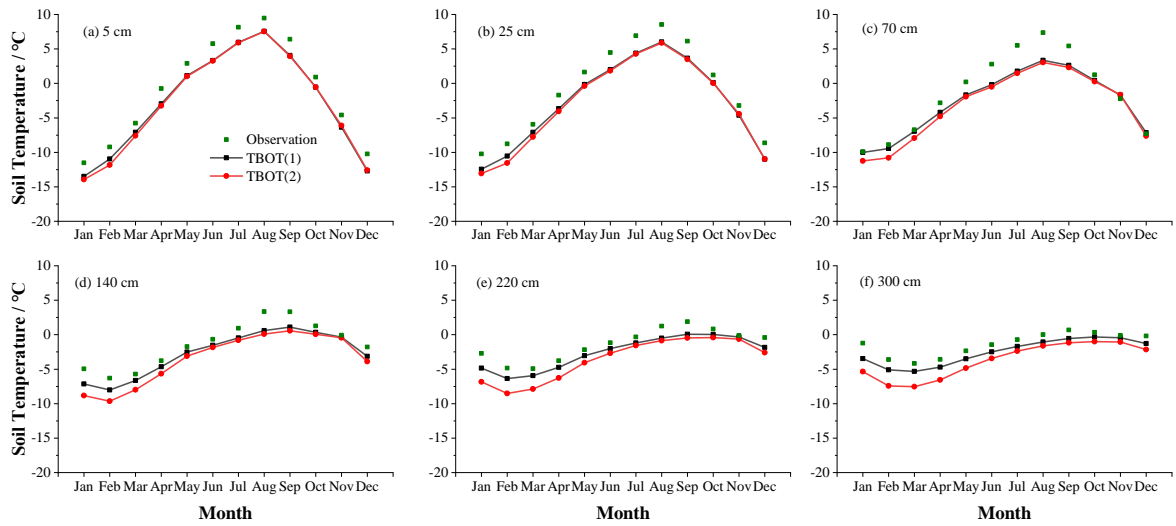
Figure. S7 Monthly soil temperature at (a) 5 cm, (b) 25 cm, (c) 70 cm, (d) 140 cm, (e) 220 cm, (f) 300 cm for the TBOT process.
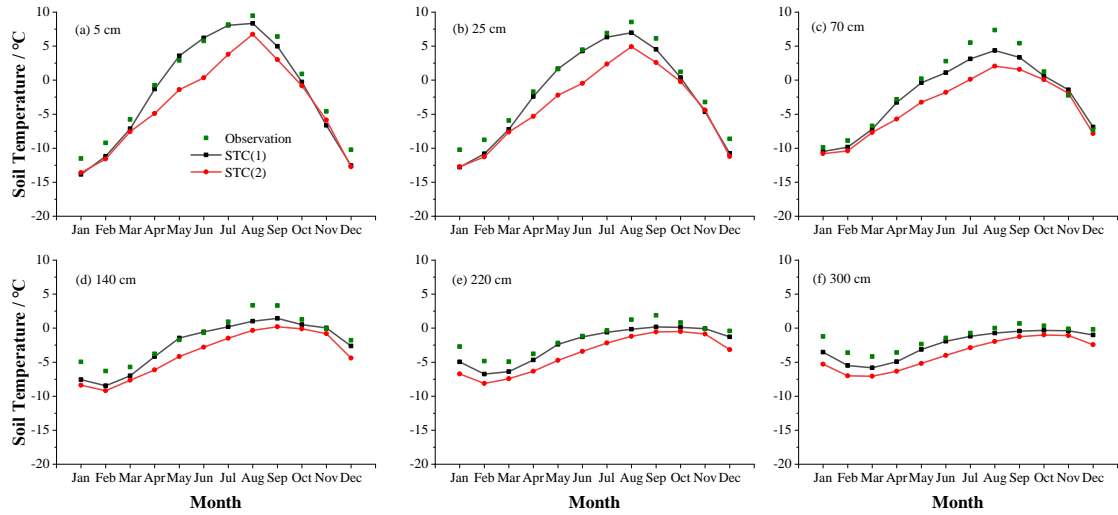
Figure. S8 Monthly soil temperature at (a) 5 cm, (b) 25 cm, (c) 70 cm, (d) 140 cm, (e) 220 cm, (f) 300 cm for the STC process.

Main findings at BLH site:

(1) Noah-MP tend to overestimate snow cover events at BLH site with large uncertainties during the cold months (Nov.-Mar). Moreover, snow cover events are mostly influenced by the STC and SUB process (Figure S11), and the combination of STC(1) and SUB(2) tend to produce better results (Figure 8). The small influence of physical processes during the warm season (Figure S11c) is because there are limited snow events, and its inability of reproducing snow cover in May (Figure S9).

(2) Noah-MP generally underestimate STs with relatively large gaps during the snow-affected months (Nov.-Mar.), and the simulated ST in the snow-affected months (Nov.-Mar.) showed relatively wide uncertainty ranges (Figure S10). STs is mostly influenced by the snow processes, i.e. the STC and SUB process (Figure S12), especially during the cold season. In the warm season, the SFC and RUN process dominate the simulation of STs (Figure S12c). The combination of roughness length for heat and under-canopy aerodynamic resistance contributes to elevated soil temperature (Figure S17).

(3) Noah-MP totally underestimate SLW at BLH site (Figure S10). The RUN process dominates the SLW at most layers simulation with limit impacts (Figure S12).
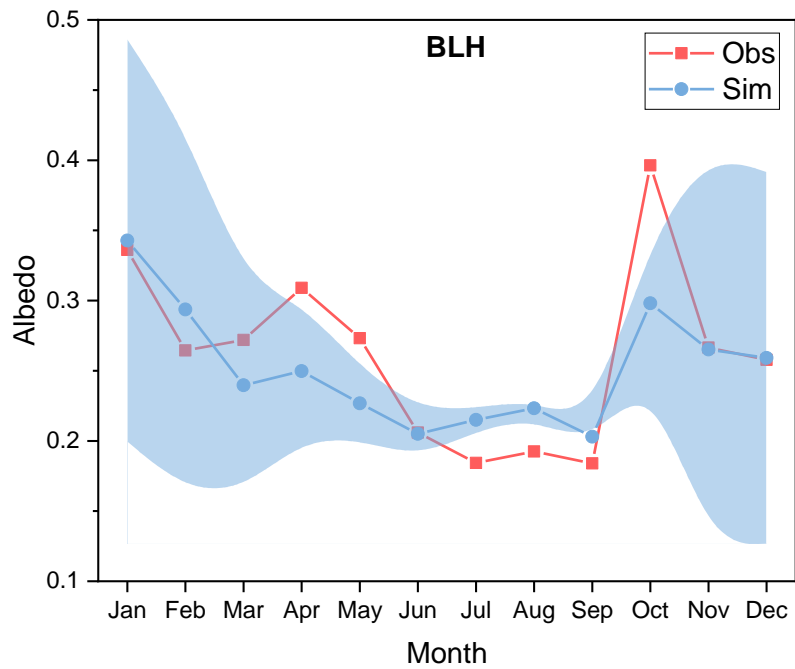
● **General performance of the ensemble simulation**

Figure S9. Monthly variations of ground albedo at BLH site for observation (Obs), and the ensemble simulation (Sim). The light blue shadow represents the standard deviation of the ensemble simulation.
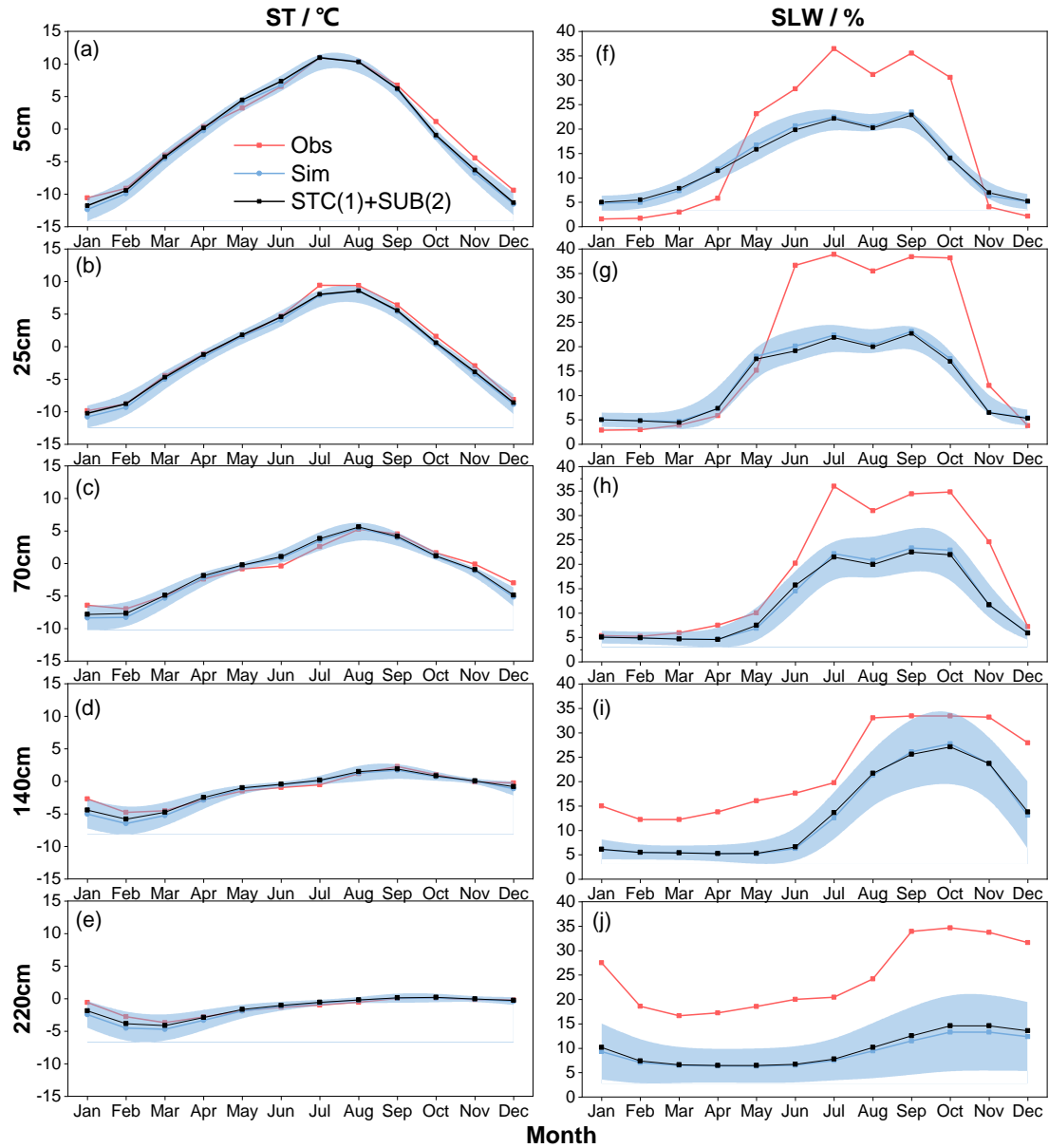
Figure S10. Monthly soil temperature (ST in °C) and soil liquid water (SLW in %) at (a, g) 5 cm, (b, h) 25 cm, (c, i) 70 cm, (d, j) 140 cm, (e, k) 220 cm, (f, l) 300 cm at BLH site. The light blue shadow represents the standard deviation of the ensemble simulation. The black line-symbol represents the ensemble mean of simulations with STC(1) and SUB(2).

● Influence degrees of physical processes
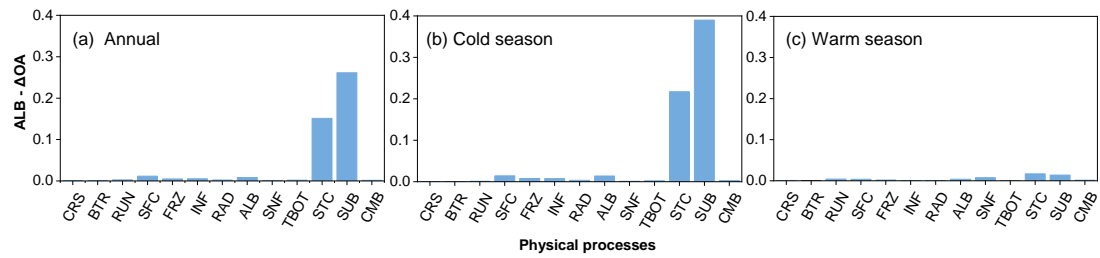
Figure S11. The maximum difference of the mean overall accuracy (OA) for albedo (ALB-ΔOA) in each physical process during the (a) annual, (b) cold season, and (c) warm season at BLH site.
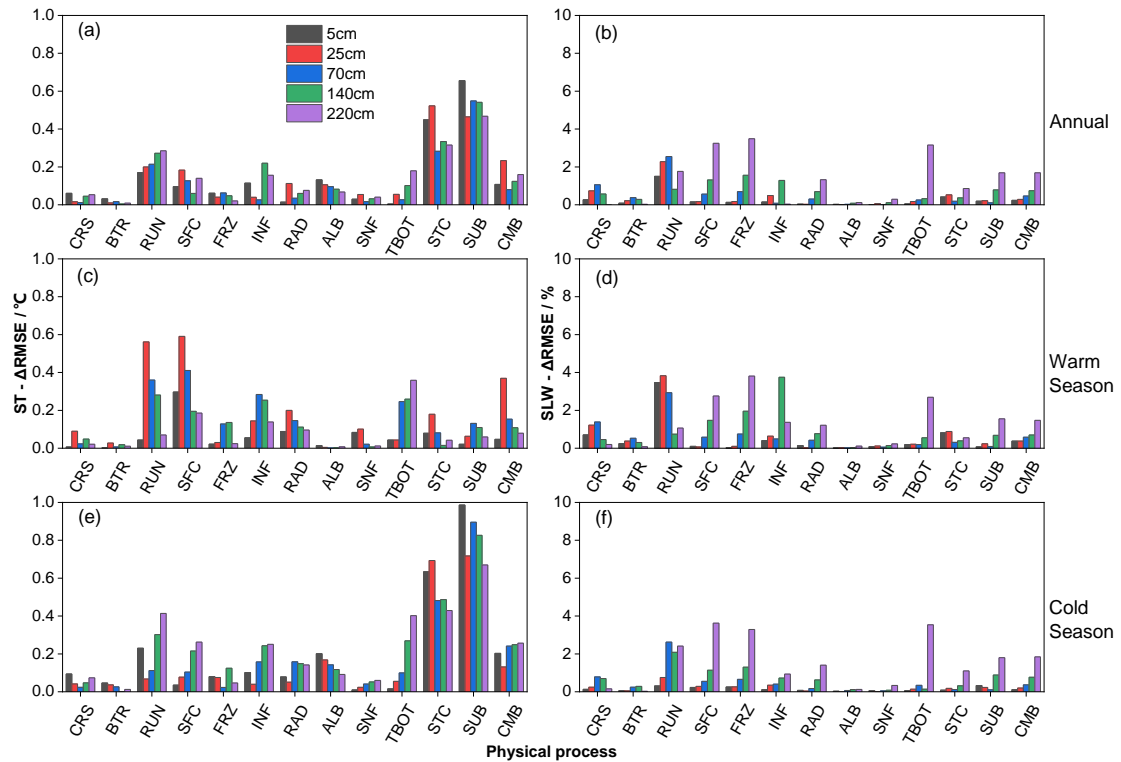
Figure S12. The maximum difference of the mean RMSE for (a, c and e) soil temperature (ST-$\Delta \overline{RMSE}$ in °C) and (b, d and f) soil liquid water (SLW-$\Delta \overline{RMSE}$ in %) in each physical process during the (a and b) annual, (c and d) warm, and (e and f) cold season at different soil depths at BLH site.

- **Sensitivities of physical processes and general behaviors of parameterizations**
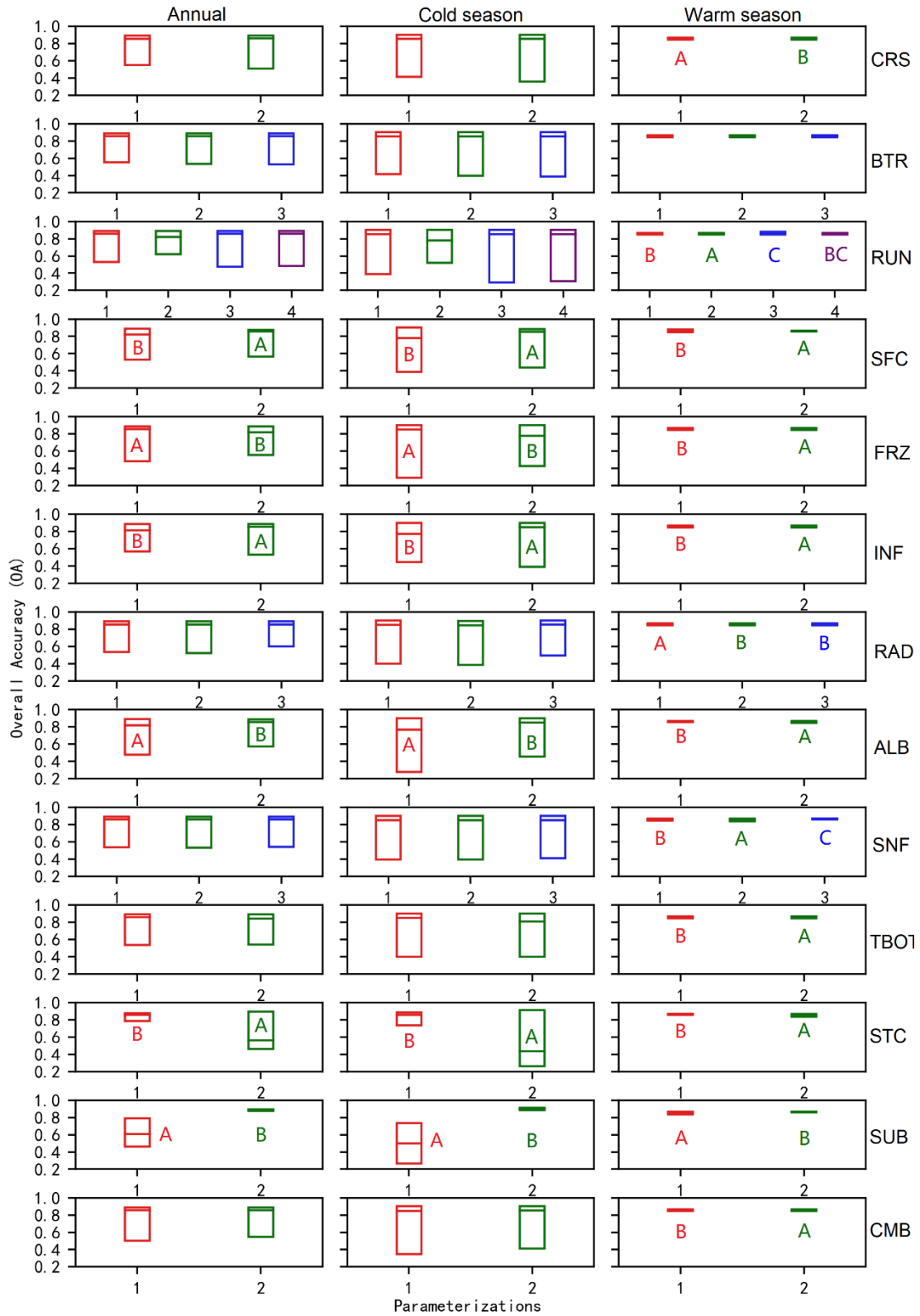
Figure S13. Distinction level for overall accuracy (OA) of snow cover events (SCEs) during the annual, warm, and cold seasons in the ensemble simulations at BLH site.
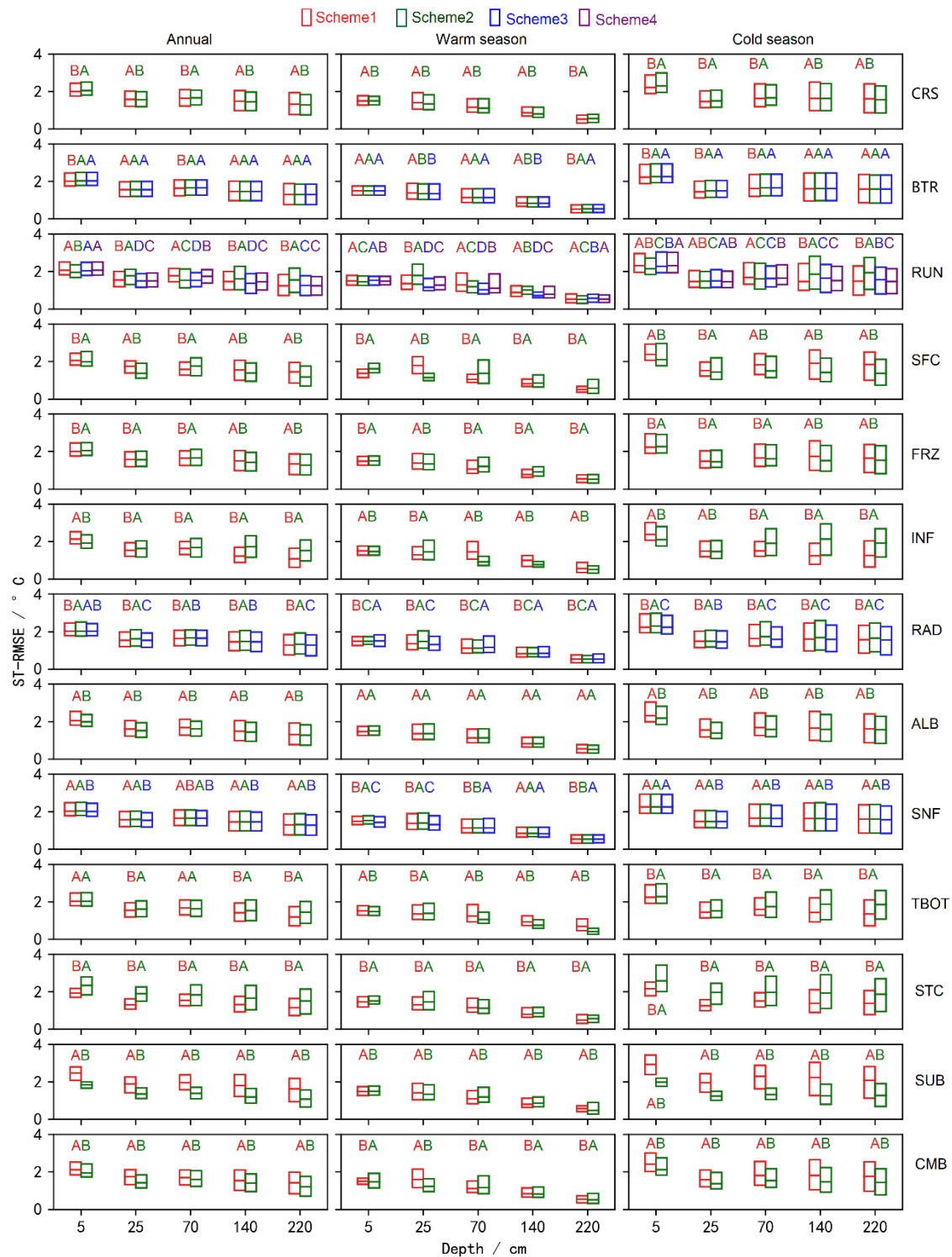
Figure S14. Distinction level for RMSE of ST at different layers during the annual, warm, and cold seasons in the ensemble simulations at BLH site. Limits of the boxes represent upper and lower quartiles, lines in the box indicate the median value.
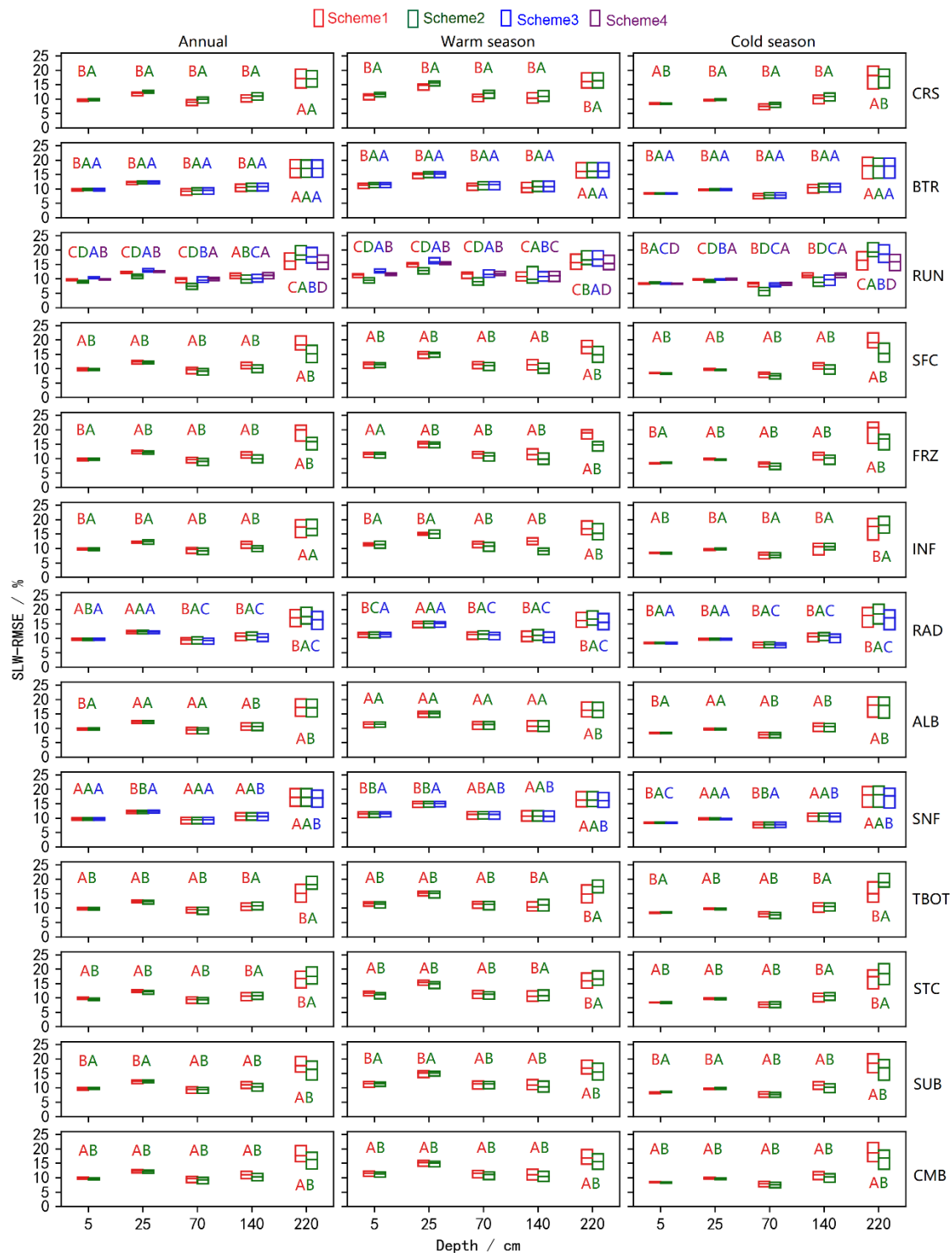
Figure S15. Distinction level for RMSE of SH2O at different layers during the annual, warm, and cold seasons in the ensemble simulations at BLH site. Limits of the boxes represent upper and lower quartiles, lines in the box indicate the median value.
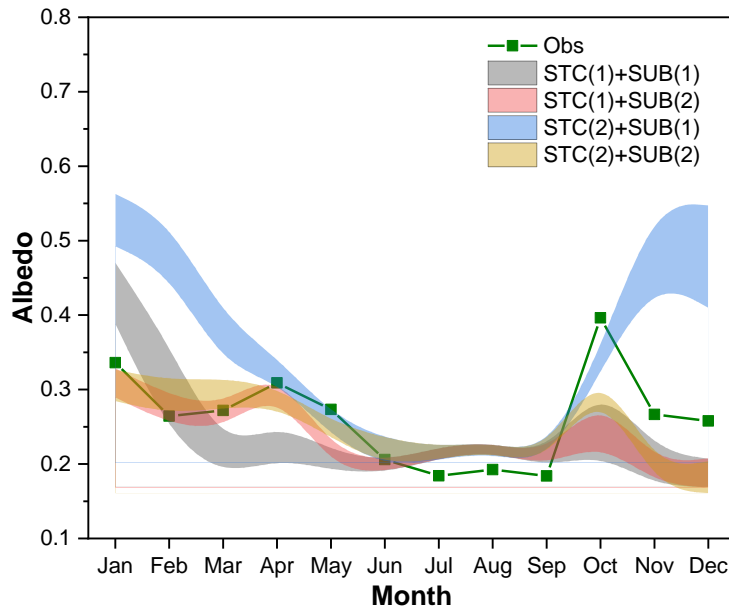
Figure S16. Uncertainty interval of ground albedo at BLH site in dominant physical processes (STC and SUB) for snow cover event simulation.
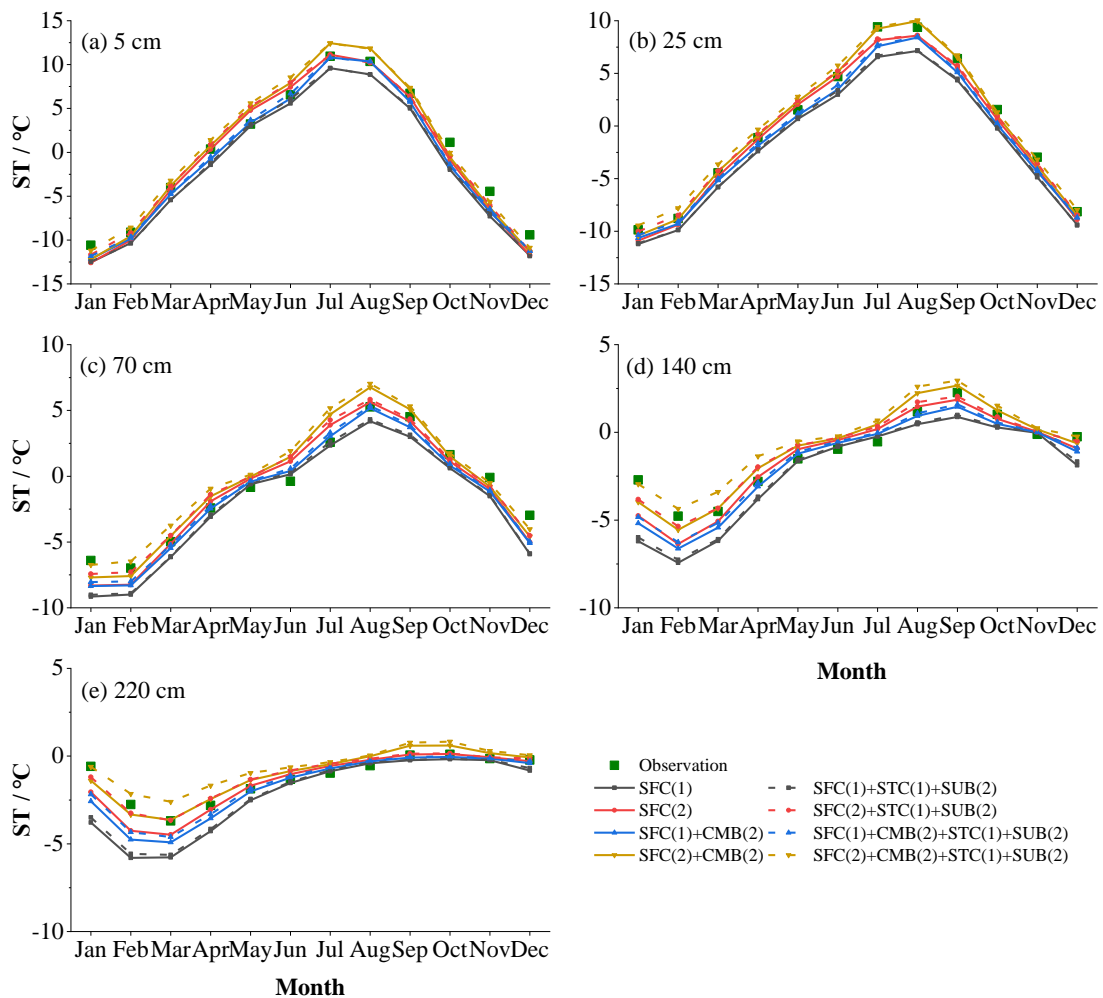

Figure S17. Monthly soil temperature (ST in °C) at (a) 5 cm, (b) 25 cm, (c) 70 cm, (d)

140 cm, (e) 220 cm, (f) 300 cm for the SFC process that consider the CMB(2) and STC(1)+SUB(2) processes or not.

References:

Hillel, D.: Applications of Soil Physics, Academic Press, 400 pp., 1980.

Cosby, B. J., Hornberger, G. M., Clapp, R. B., and Ginn, T. R.: A Statistical Exploration of the Relationships of Soil Moisture Characteristics to the Physical Properties of Soils, Water Resour. Res., 20, 682-690, https://doi.org/10.1029/WR020i006p00682, 1984.

Wetzel, P., and Chang, J.-T.: Concerning the Relationship between Evapotranspiration and Soil Moisture, J. Clim. Appl. Meteorol., 26, 18-27, https://doi.org/10.1175/1520-0450(1987)026<0018:CTRBEA>2.0.CO;2, 1987.